Three Long-period Transiting Giant Planets from TESS[*]

Rafael Brahm[1,2,3], Solène Ulmer-Moll[4,5], Melissa J. Hobson[2,6], Andrés Jordán[1,2,3], Thomas Henning[6],
Trifon Trifonov[6,7], Matías I. Jones[8], Martin Schlecker[9], Nestor Espinoza[10], Felipe I. Rojas[2,11], Pascal Torres[2,11],
Paula Sarkis[6], Marcelo Tala[1], Jan Eberhardt[6], Diana Kossakowski[6], Diego J. Muñoz[1,12], Joel D. Hartman[13],
Gavin Boyle[14,15], Vincent Suc[1,16], François Bouchy[5], Adrien Deline[5], Guillaume Chaverot[5], Nolan Grieves[5],
Monika Lendl[5], Olga Suarez[17], Tristan Guillot[17], Amaury H. M. J. Triaud[18], Nicolas Crouzet[19],
Georgina Dransfield[18], Ryan Cloutier[20,21], Khalid Barkaoui[22,23,24], Rick P. Schwarz[21], Chris Stockdale[25],
Mallory Harris[26], Ismael Mireles[26], Phil Evans[14], Andrew W. Mann[27], Carl Ziegler[28], Diana Dragomir[29],
Steven Villanueva[30], Christoph Mordasini[31], George Ricker[32], Roland Vanderspek[32], David W. Latham[21],
Sara Seager[32,33,34], Joshua N. Winn[13], Jon M. Jenkins[35], Michael Vezie[32], Allison Youngblood[36], Tansu Daylan[13,40],
Karen A. Collins[21], Douglas A. Caldwell[37], David R. Ciardi[38], Enric Palle[24], and Felipe Murgas[24,39]

[1] Facultad de Ingeniera y Ciencias, Universidad Adolfo Ibáñez, Av. Diagonal las Torres 2640, Peñalolén, Santiago, Chile; rafael.brahm@uai.cl
[2] Millennium Institute for Astrophysics, Chile
[3] Data Observatory Foundation, Chile
[4] Physikalisches Institut, University of Bern, Gesellsschaftsstrasse 6, 3012 Bern, Switzerland
[5] Observatoire astronomique de l'Université de Genève, chemin Pegasi 51, 1290 Versoix, Switzerland
[6] Max-Planck-Institut für Astronomie, Königstuhl 17, D-69117 Heidelberg, Germany
[7] Department of Astronomy, Sofia University "St Kliment Ohridski," 5 James Bourchier Boulevard, BG-1164 Sofia, Bulgaria
[8] European Southern Observatory, Casilla 19001, Santiago, Chile
[9] Steward Observatory and Department of Astronomy, The University of Arizona, Tucson, AZ 85721, USA
[10] Space Telescope Science Institute, 3700 San Martin Drive, Baltimore, MD 21218, USA
[11] Instituto de Astrofísica, Facultad de Física, Pontificia Universidad Católica de Chile, Chile
[12] Center for Interdisciplinary Exploration and Research in Astrophysics (CIERA) and Department of Physics and Astronomy, Northwestern University, 2145
Sheridan Road, Evanston, IL 60208, USA
[13] Department of Astrophysical Sciences, Princeton University, 4 Ivy Lane, Princeton, NJ 08544, USA
[14] El Sauce Observatory, Coquimbo Province, Chile
[15] Cavendish Laboratory, J J Thomson Avenue, Cambridge, CB3 0HE, UK
[16] El Sauce Observatory—Obstech, Chile
[17] Université Côte d'Azur, Observatoire de la Côte d'Azur, CNRS, Laboratoire Lagrange, Bd de l'Observatoire, CS 34229, F-06304 Nice cedex 4, France
[18] School of Physics & Astronomy, University of Birmingham, Edgbaston, Birmingham B15 2TT, UK
[19] European Space Agency (ESA), European Space Research and Technology Centre (ESTEC), Keplerlaan 1, 2201 AZ Noordwijk, The Netherlands
[20] Dept. of Physics & Astronomy, McMaster University, 1280 Main Street West, Hamilton, ON L8S 4L8, Canada
[21] Center for Astrophysics | Harvard & Smithsonian, 60 Garden Street, Cambridge, MA 02138, USA
[22] Astrobiology Research Unit, Université de Liège, Allée du 6 Août 19C, B-4000 Liège, Belgium
[23] Department of Earth, Atmospheric and Planetary Science, Massachusetts Institute of Technology, 77 Massachusetts Avenue, Cambridge, MA 02139, USA
[24] Instituto de Astrofísica de Canarias (IAC), E-38200 La Laguna, Tenerife, Spain
[25] Hazelwood Observatory, Australia
[26] Department of Physics and Astronomy, University of New Mexico, 210 Yale Boulevard NE, Albuquerque, NM 87106, USA
[27] Department of Physics and Astronomy, The University of North Carolina at Chapel Hill, Chapel Hill, NC 27599, USA
[28] Department of Physics, Engineering and Astronomy, Stephen F. Austin State University, 1936 North Street, Nacogdoches, TX 75962, USA
[29] Department of Physics and Astronomy, University of New Mexico, 1919 Lomas Boulevard NE, Albuquerque, NM 87131, USA
[30] NASA Goddard Space Flight Center, Exoplanets and Stellar Astrophysics Laboratory (Code 667), Greenbelt, MD 20771, USA
[31] Center for Space and Habitability, Universitat Bern, Gesellshaftsstrasse 6, 3012 Bern, Switzerland
[32] Department of Physics and Kavli Institute for Astrophysics and Space Research, Massachusetts Institute of Technology, Cambridge, MA 02139, USA
[33] Department of Earth, Atmospheric and Planetary Sciences, Massachusetts Institute of Technology, Cambridge, MA 02139, USA
[34] Department of Aeronautics and Astronautics, MIT, 77 Massachusetts Avenue, Cambridge, MA 02139, USA
[35] NASA Ames Research Center, Moffett Field, CA 94035, USA
[36] NASA Goddard Space Flight Center, 8800 Greenbelt Road, Greenbelt, MD 20771, USA
[37] SETI Institute/NASA Ames Research Center, USA
[38] Caltech/IPAC-NASA Exoplanet Science Institute, 770 S. Wilson Avenue, Pasadena, CA 91106, USA
[39] Departamento de Astrofísica, Universidad de La Laguna (ULL), E-38206 La Laguna, Tenerife, Spain

Abstract

We report the discovery and orbital characterization of three new transiting warm giant planets. These systems
were initially identified as presenting single-transit events in the light curves generated from the full-frame images
of the Transiting Exoplanet Survey Satellite. Follow-up radial velocity measurements and additional light curves

were used to determine the orbital periods and confirm the planetary nature of the candidates. The planets orbit slightly metal-rich late F- and early G-type stars. We find that TOI 4406b has a mass of $M_P = 0.30 \pm 0.04\,M_J$, a radius of $R_P = 1.00 \pm 0.02\,R_J$, and a low-eccentricity orbit ($e = 0.15 \pm 0.05$) with a period of $P = 30.08364 \pm 0.00005$ days. TOI 2338b has a mass of $M_P = 5.98 \pm 0.20\,M_J$, a radius of $R_P = 1.00 \pm 0.01\,R_J$, and a highly eccentric orbit ($e = 0.676 \pm 0.002$) with a period of $P = 22.65398 \pm 0.00002$ days. Finally, TOI 2589b has a mass of $M_P = 3.50 \pm 0.10\,M_J$, a radius of $R_P = 1.08 \pm 0.03\,R_J$, and an eccentric orbit ($e = 0.522 \pm 0.006$) with a period of $P = 61.6277 \pm 0.0002$ days. TOI 4406b and TOI 2338b are enriched in metals compared to their host stars, while the structure of TOI 2589b is consistent with having similar metal enrichment to its host star.

Unified Astronomy Thesaurus concepts: Exoplanets (498); Extrasolar gaseous giant planets (509); Radial velocity (1332); Transit photometry (1709)

Supporting material: machine-readable table

1. Introduction

In the past couple of decades astronomers have started to uncover the different types of planets that orbit stars other than the Sun, finding that the solar system architecture is just one of the many possible outcomes of the planet formation process (see Winn & Fabrycky 2015, for a detailed review). Among the new types of planets identified, gas giant planets with short orbits (e.g., Mayor & Queloz 1995; Bakos et al. 2007) stand out because they were not expected to exist according to classical models of planet formation (e.g., Stevenson 1982). While advances have been made in observational and theoretical aspects, the formation mechanism of this planet population is still an unsolved puzzle.

If these planets were not formed at their current locations, they should have migrated from beyond the snowline. One possible migration scenario involves the loss of angular momentum through torques with the gaseous disk as long as it is still present (e.g., Goldreich & Tremaine 1980; Lin & Papaloizou 1986). Another possible migration mechanism is through gravitational interactions with a third body that excites the orbital eccentricity, which generates orbital shrinking due to tidal interactions with the star during periastron passages (e.g., Rasio & Ford 1996; Wu & Lithwick 2011).

These two types of migration processes predict different outcomes in terms of orbital parameters for the inner planet. Specifically, ongoing high-eccentricity migration mechanisms predict a wide distribution for the orbital eccentricities and obliquities (e.g., Chatterjee et al. 2008), while disk migration by itself mostly predicts circular orbits aligned with the stellar spin. Additionally, the bulk structures and atmospheric compositions of these planets can be related to formation locations in the disk and possible migration paths (Madhusudhan et al. 2014; Mollière et al. 2022). The detection and detailed characterization of the physical and orbital properties of close-in giant planets are crucial for constraining their formation and migration scenarios. In this regard, those giant planets that transit bright stars are particularly valuable because of the amount of information that can be obtained.

Hot Jupiters, broadly defined as giant planets with orbital periods shorter than 10 days, have been efficiently characterized in the past decades (see Dawson & Johnson 2018, for a detailed review), allowing one to get some constraints on the main migration mechanisms involved in their orbital evolution (e.g., Rice et al. 2022a). Nonetheless, due to their extreme proximity to the star, conclusions based on this population can be affected by posterior radiative and tidal interactions with the star (e.g., Albrecht et al. 2012). On the other hand, giant planets

with orbital periods longer than 10 days but inside the snowline are not subject to strong proximity effects, which allows one to perform a more direct comparison of their properties to those predicted by the different formation/migration scenarios (e.g., Huang et al. 2016). For example, the mass and radius of warm Jupiters can be used to infer the bulk internal structure and composition of the planet through the use of standard interior models (Espinoza et al. 2017). Additionally, the obliquity angle measured for warm Jupiters through the Rossiter–McLaughlin effect can be used to constrain migration models (Morton & Johnson 2011).

While ground-based photometric surveys have been successful in the detection of transiting hot Jupiters around bright stars, those having periods longer than ∼8 days, with some particular exceptions (e.g., HATS-17b; Brahm et al. 2016), remained mostly elusive to these projects owing to the diurnal cycle. The NASA Kepler mission started to expand the parameter space of well-characterized giant planets by discovering some candidates orbiting stars bright enough for radial velocity measurements to determine their masses (Almenara et al. 2015; Dalba et al. 2021a, 2021b; Chachan et al. 2022). Nonetheless, due to its increased field of view compared to that of the NASA Kepler mission, the Transiting Exoplanet Survey Satellite (TESS; Ricker et al. 2015) is enabling for the first time the systematic exploration and characterization of the domain of transiting warm Jupiters, either through the detection of periodic transiting signals or through the detection of single transiters (e.g., Gill et al. 2020; Dawson et al. 2021; Dong et al. 2021a; Eisner et al. 2021; Dalba et al. 2022; Grieves et al. 2022). The brightness of the stars monitored by TESS allows a detailed dynamical characterization to be obtained via the measurement of precision radial velocities. In this context, the Warm gIaNts with TESS (WINE) collaboration is currently performing a dedicated survey to identify, confirm, and characterize warm giant planets using as a starting point the TESS data (Brahm et al. 2019, 2020; Jordán et al. 2020; Schlecker et al. 2020; Hobson et al. 2021; Trifonov et al. 2021).

In this study, we present the discovery, confirmation, and orbital characterization of three new transiting warm giant planets initially identified as community TESS objects of interest (cTOIs) by the WINE collaboration and subsequently adopted by the TESS project as project TOIs. We have utilized ground-based spectroscopic and photometric observations to confirm these planetary candidates as three new warm giant planets.
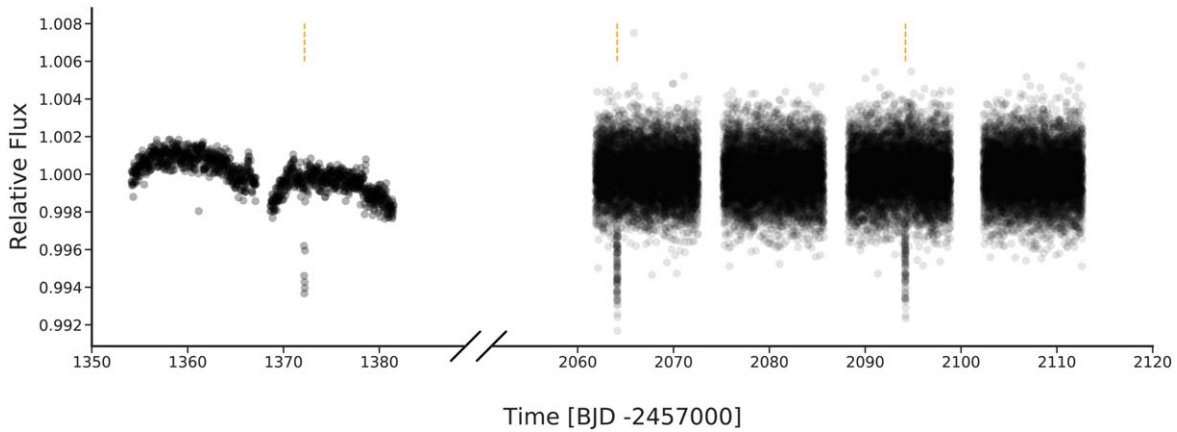
Figure 1. TESS light curves of TOI 4406. Dashed vertical lines indicate the transits that were identified.

2. Observations

2.1. TESS

All three transiting candidates presented in this study were identified from the full-frame image (FFI) light curves of the TESS primary mission. The FFIs were calibrated by the Science Processing Operations Center (SPOC) at NASA Ames Research Center (Jenkins et al. 2016). As the WINE collaboration, we generate light curves through the `tesseract`[41] pipeline for all stars brighter than $T = 13$ mag of all TESS sectors soon after the data are made public. Due to our focus on the detection of giant transiting giant planets in long-period orbits ($P > 10$ days), we process all the light curves with a dedicated algorithm that, after passing them through a median filter, identifies systematic negative deviations in flux, whose amplitudes could be consistent with the depths and durations of transits of giant planets orbiting main-sequence/subgiant stars. All systems that present such specific variations are then manually vetted. The light curves from which the long-period candidates are identified are not corrected for flux contamination of neighboring stars by `tesseract`. The possible dilution of the transits by neighboring stars that fall inside the TESS photometric aperture is considered in the manual vetting process when estimating the planet radius from the transit depth and host stellar radius.

TOI 4406 was observed by TESS in sector 2. An ≈5100 ppm single transit was identified with a duration of ≈0.16 days. A query to the Gaia DR2 (Gaia Collaboration et al. 2018) archive revealed that this target presented no neighboring stars closer than 30″ and a small uncertainty in the radial velocity measurements (0.6 km s^{-1}), and therefore it was selected as a high-priority candidate of the WINE collaboration, suitable for spectroscopic follow up.

TOI 2338 was observed by TESS in sectors 5 and 6. A single transiter candidate was identified in the `tesseract` light curve of sector 5. The transit-like signal presented a depth of ≈11,000 ppm and a duration of 0.17 days. As soon as the FFIs of sector 6 were made public, we generated the corresponding light curve for TOI 2338 and identified a second transit with similar properties to those of sector 5. The transits were separated by 22.7 days. Gaia DR2 reports just one faint neighboring star closer than 30″ for TOI 2338 and a small

radial velocity uncertainty (0.6 km s^{-1}), and therefore this system was also classified as a high-priority WINE candidate.

TOI 2589 was observed by TESS in sector 7. In its `tesseract` light curve we identified a single transiter with a depth of ≈9000 ppm and a duration of 0.28 days. As opposed to the other two candidates, TOI 2589 presented nine neighboring stars closer than 30″ according to the Gaia DR2 catalog. Nonetheless, all of them were relatively faint in comparison to TOI 2589. The reported radial velocity uncertainty was small (0.6 km s^{-1}), and this system was also selected as a high-priority candidate.

Due to their promising properties, we proposed these three systems (along with others) to be observed in Cycle 3 of the TESS mission in 2 m cadence mode in order to further constrain the transiting parameters and determine the orbital periods of the candidates orbiting TOI 4406 and TOI 2589. Therefore, in the first year of the TESS extended mission, additional TESS light curves were obtained for these three systems. TOI 4406 was observed in 2 m cadence mode in sectors 28 and 29, presenting one additional transit in each light curve. TOI 2338 was observed in sector 32 in 2 m cadence mode, and one additional transit was identified for this candidate. Finally, TOI 2589 was observed by TESS in 2 m mode in sectors 33 and 34, and an additional transit was identified in sector 34. These new TESS data unambiguously constrained the periods of TOI 4406 and TOI 2338 to be 30.08 and 22.65 days, respectively, but were not enough to determine an exact orbital period for TOI 2589, for which additional data were required.

All these 2 m cadence observations were processed by the SPOC pipeline (Twicken et al. 2018). For TOI 4406 the SPOC search of sectors 28 and 29 generated a clean data validation report and the transit signature passed all the diagnostic tests, including the difference imaging centroiding test, which located the source of the transits to within 1″233 ± 2″6804 of the target star's catalog position. For TOI 2338 the SPOC search of sector 34 identified the single transit and the difference image centroiding test located the source of the transit to within 0″3 ± 2″5 of the catalog star position. Finally, for TOI 2589 the SPOC search of sector 32 identified the single transit and the difference image centroiding test located the source of the transit to within 0″35 ± 2″7 of the catalog star position.

Figures 1, 2, and 3 show all TESS light curves with transits for TOI 4406, TOI 2338, and TOI 2589, respectively.
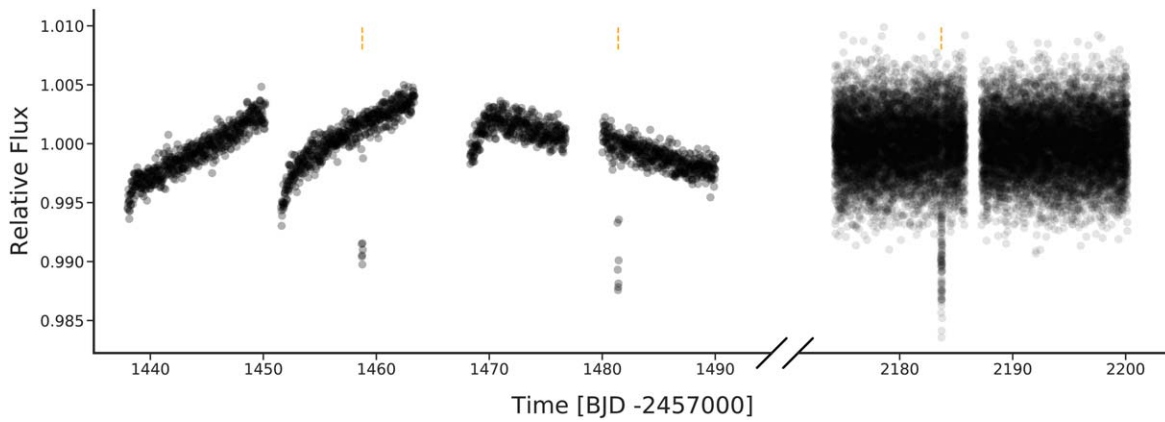
Figure 2. TESS light curves of TOI 2338. Dashed vertical lines indicate the transits that were identified.
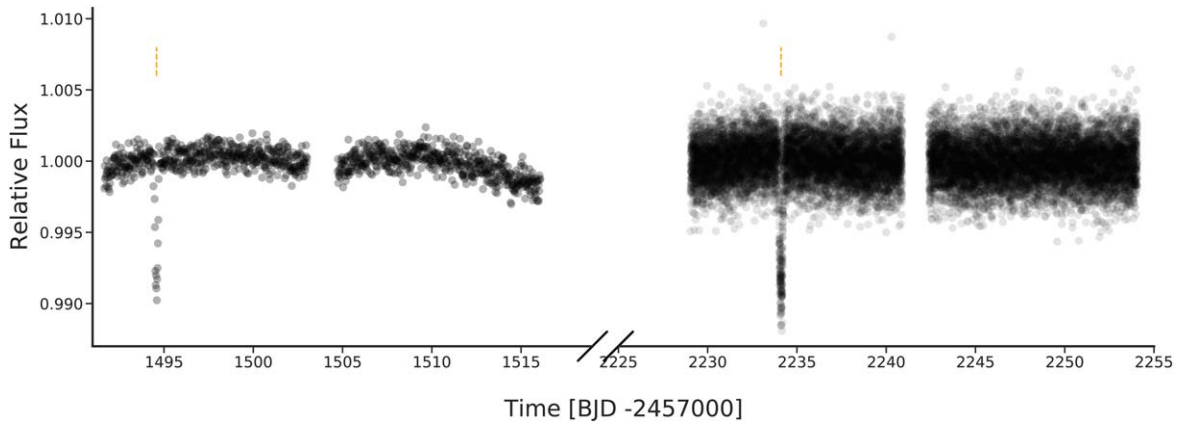

Figure 3. TESS light curves of TOI 2589. Dashed vertical lines indicate the transits that were identified.

Table 1
Radial Velocity Measurements for TOI 4406, TOI 2338, and TOI 2589

ID	BJD −2,450,000	RV (m s^{-1})	σ_{RV} (m s^{-1})	BIS (m s^{-1})	σ_{BIS} (m s^{-1})	S_{index}	Instrument
TOI 4406b	8638.90562	24,211.8	10.5	1.0	12.0	0.138 ± 0.013	FEROS
TOI 4406b	8643.92198	24,161.3	9.4	32.0	11.0	0.173 ± 0.011	FEROS
TOI 4406b	8657.87399	24,189.2	8.6	−9.0	10.0	0.140 ± 0.009	FEROS
TOI 4406b	8669.78376	24,237.9	10.3	18.0	11.0	0.135 ± 0.012	FEROS
TOI 4406b	8672.86255	24,195.5	13.6	−6.0	14.0	0.151 ± 0.018	FEROS
TOI 4406b	8674.83206	24,222.9	10.9	−1.0	12.0	0.107 ± 0.012	FEROS
TOI 4406b	8677.80976	24,176.6	9.0	3.0	10.0	0.139 ± 0.009	FEROS
TOI 4406b	8718.74463	24,163.7	8.4	17.0	10.0	0.142 ± 0.008	FEROS
TOI 2589b	8814.78468	68,294.7	6.6	−19.0	11.0	0.146 ± 0.010	FEROS
TOI 2589b	8815.78744	68,370.8	6.9	−32.0	11.0	0.182 ± 0.011	FEROS
TOI 2589b	8907.71907	68,634.2	8.8	26.0	13.0	0.184 ± 0.020	FEROS
TOI 2589b	8909.64069	68,631.8	7.5	−9.0	11.0	0.139 ± 0.012	FEROS
TOI 2589b	8914.63041	68,563.7	9.1	−18.0	13.0	0.165 ± 0.017	FEROS
TOI 2589b	8922.59456	68,491.6	10.9	9.0	15.0	0.176 ± 0.023	FEROS
TOI 2338b	8916.59777	83,777.2	10.3	−31.0	15.0	0.229 ± 0.023	FEROS
TOI 2338b	8917.57140	83,708.0	9.8	−27.0	14.0	0.219 ± 0.023	FEROS
TOI 2338b	8918.53080	83,697.1	8.2	1.0	12.0	0.163 ± 0.016	FEROS
TOI 2338b	8928.56100	83,906.9	12.9	1.0	18.0	0.154 ± 0.041	FEROS
TOI 2338b	8929.57890	83,985.2	8.2	5.0	12.0	0.173 ± 0.017	FEROS
TOI 2338b	9180.61110	84,186.1	5.5	15.0	7.0	0.033 ± 0.013	HARPS
TOI 2338b	9182.66670	84,918.6	6.7	5.0	9.0	-0.008 ± 0.014	HARPS

Note. This table is available in a machine-readable form in the online journal. A portion is shown here for guidance regarding its form and content.

(This table is available in its entirety in machine-readable form.)
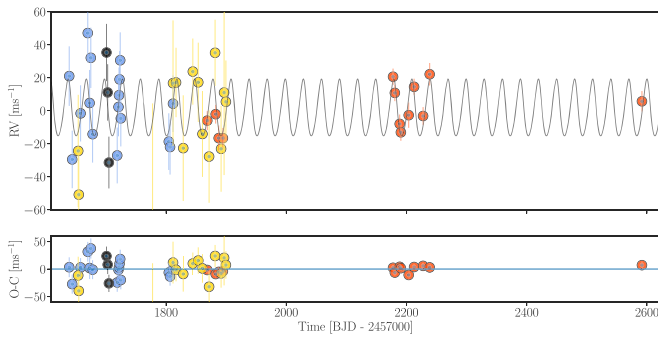
Figure 4. Radial velocities of TOI 4406 obtained with FEROS (blue), Coralie (yellow), CHIRON (black), and HARPS (orange).

Figure 6. Radial velocities of TOI 2589 obtained with FEROS (blue), CHIRON (black), HARPS (orange), and CORALIE (yellow).
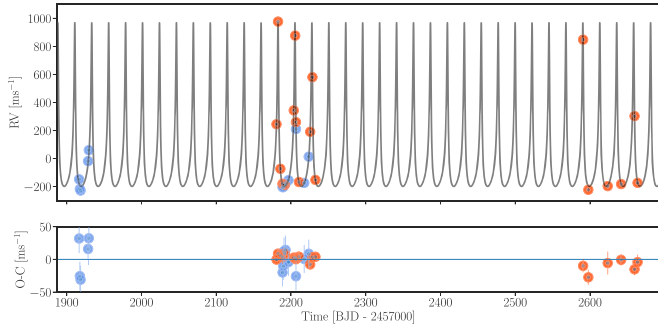
Figure 5. Radial velocities of TOI 2338 obtained with FEROS (blue) and HARPS (orange).

2.2. Spectroscopy

Our three targets of interest were followed up spectroscopically with four different instruments installed in the north of Chile. The goal of these follow-up observations was to measure precision radial velocities and search for variations consistent with the planetary hypothesis for the transiting signals. All the radial velocities obtained for our three systems are presented in Table 1. The radial velocity measurements are also presented in Figures 4, 5, and 6, for TOI 4406, TOI 2338, and TOI 2589, respectively.

2.2.1. FEROS

The Fiber-fed, Extended Range, Échelle Spectrograph (FEROS; Kaufer et al. 1999) is a bench-mounted, thermally controlled, prism-cross-dispersed echelle spectrograph, currently installed in the MPG 2.2 m telescope at the ESO La Silla Observatory, in Chile. It has a spectral resolution of $R \approx 48,000$, high efficiency (20%), and a spectral coverage from 350 to 920 nm divided into 39 echelle orders. FEROS was the first instrument to be used in the spectroscopic follow up of the three systems presented in this study. All FEROS observations associated with the WINE collaboration are performed with the simultaneous calibration mode (Baranne et al. 1996) for tracing instrumental velocity drift variations in the spectrograph enclosure due to changes in its environment (mostly temperature and atmospheric pressure changes).

TOI 4406 was observed on 16 different epochs between 2019 June and November. The adopted exposure time was 600 s, which delivered spectra with signal-to-noise ratios per resolution element in the range of 50–100 depending on the specific observing conditions of each night.

TOI 2338 was observed on 13 different nights with FEROS starting in 2020 March and taking the last spectrum in 2021
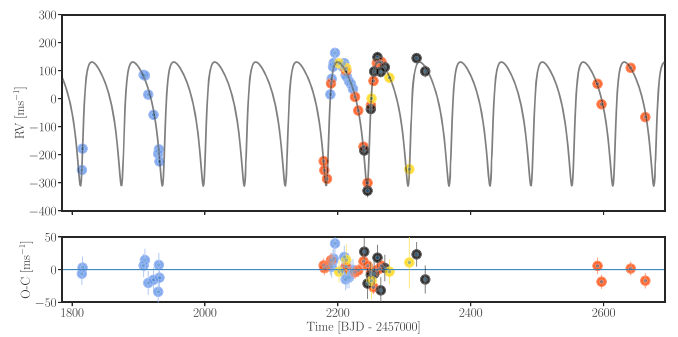
January. The exposure time was set to 1200 s for this target, and we obtained spectra with signal-to-noise ratios between 50 and 80.

We obtained 21 FEROS spectra of TOI 2589 between 2019 November and 2021 January. In this case we adopted an exposure time of 900 s, which translated to a typical signal-to-noise ratio of 80.

All FEROS data obtained for this study were processed with the `ceres` pipeline (Brahm et al. 2017a). `ceres` performs all the reduction steps to generate a continuum-normalized, wavelength-calibrated, and optimally extracted spectrum from raw data. `ceres` also computes precision radial velocities and bisector span measurements through the cross-correlation technique. A G2-type binary mask was used as a template for computing the cross-correlation function of the spectra of our three candidates.

FEROS radial velocities for TOI 4406 indicated that some time-correlated variations were present but with an amplitude not much larger than the radial velocity uncertainties. For TOI 2338, FEROS radial velocities quickly showed significant variations in phase with the 22-day orbital period of the transiting candidate, with an amplitude that could be produced by a giant planet. Finally, FEROS radial velocities for TOI 2589 also showed variations that could be produced by a massive planet, and after some months of observations, we were able to constrain the orbital period of this single-transit candidate from these radial velocities.

2.2.2. HARPS

The High Accuracy Radial velocity Planet Searcher (HARPS; Mayor et al. 2003) is a high-resolution and stabilized spectrograph fiber-fed by the Cassegrain focus of the ESO 3.6 m telescope of the ESO La Silla Observatory, in Chile. It covers the spectral region of 380–690 nm, with a resolving power of $R = 115,000$. We decided to use HARPS to follow up our three systems, for different reasons. The amplitude of the tentative radial velocity variations that we identified with FEROS for TOI 4406 was too shallow to tightly constrain a possible orbit. In the case of TOI 2338, even though the amplitude of the radial velocity signal was significantly larger, we did not have access to FEROS during the orbital phase close to periastron, so that the eccentricity was significantly unconstrained with the FEROS data alone. Finally, for TOI 2589, we initially identified a second small-amplitude variation in addition to the one linked to the transiting planet, and we were interested to see whether we could constrain it with HARPS radial velocities. All HARPS data for this work

Table 2
Summary of Ground-based Follow-up Observations of TOI 4406, TOI 2338, and TOI 2589

Target	Observatory	Date	Aperture (m)	Filter	Exposure Time (s)
TOI 4406b	LCO-SAAO	2020-10-31	1.0	ip	60
TOI 4406b	LCO-SSO	2021-08-28	1.0	B	25
TOI 4406b	LCO-SSO	2021-08-28	1.0	zs	37
TOI 4406b	ASTEP	2021-09-27	0.4	Rc	60
TOI 2338b	El Sauce	2020-11-30	0.36	Rc	90
TOI 2338b	LCO-SAAO	2020-12-22	1.0	ip	145
TOI 2338b	El Sauce	2021-02-06	0.36	Rc	180
TOI 2338b	ASTEP	2021-09-20	0.4	gp	200
TOI 2338b	LCO-CTIO	2021-10-12	1.0	ip	27
TOI 2338b	LCO-CTIO	2021-10-12	1.0	gp	41
TOI 2338b	LCO-SAAO	2021-11-04	1.0	gp	41
TOI 2338b	LCO-SAAO	2021-11-04	1.0	ip	27
TOI 2589b	Hazelwood	2021-01-19	0.32	Rc	90
TOI 2589b	El Sauce (OM-ES)	2022-03-26	0.6	rp	9

were processed with the `ceres` pipeline using the same binary mask that was used for the processing of FEROS data.

We obtained 13 HARPS spectra of TOI 4406 between 2020 January and 2022 January. We adopted an exposure time of 1200 s for these observations, which yielded spectra with a signal-to-noise ratio of 55. TOI 2338 was observed on 18 different epochs, between 2020 November and 2022 April. The adopted exposure time for this object was 1200 s, which resulted in a typical signal-to-noise ratio of 30. Finally, TOI 2589 was observed 19 times with HARPS between 2020 November and 2022 April. The resulting spectra presented signal-to-noise ratios around 45, which was obtained with an exposure time of 900 s.

2.2.3. CHIRON

CHIRON is a high-resolution spectrograph installed in the 1.5 m telescope at the Cerro Tololo Inter-American Observatory (CTIO). We obtained three spectra of TOI 4406 with the CHIRON high-resolution spectrograph (Tokovinin et al. 2013) in 2019 August. The data were obtained with the image slicer ($R \sim 80,000$) and an exposure time of 1800 s, leading to a signal-to-noise ratio per pixel of ~ 20 at 550 nm. Similarly, we collected a total of 15 spectra of TOI 2589 between 2021 January 24 and 2022 January 18. The adopted exposure time was also 1800 s. In the two cases we obtained a ThAr spectrum immediately before the science spectra to account for the instrument night drift. The data were reduced by the CHIRON pipeline (Paredes et al. 2021), and the radial velocities were computed using an updated version of the pipeline used in Jones et al. (2019).

2.2.4. CORALIE

The Swiss 1.2 m Leonhard Euler Telescope installed at the ESO La Silla Observatory hosts the high-resolution CORALIE spectrograph (Queloz et al. 2000). CORALIE works at a resolution of $R = 60,000$ and uses the simultaneous calibration technique by allowing the science exposures to count with a second fiber illuminated by the spectrum of a thorium argon lamp or by a Fabry–Perot system. We obtained 18 CORALIE spectra of TOI 4406 using an exposure time of 1200 s and five spectra of TOI 2589 with an exposure time of 1800 s. The selected comparison source was the Fabry–Perot system, and the data were processed with the standard Data Reduction Software (DRS) of the instrument.

2.3. Ground-based Photometry

Ground-based photometric time series obtained with submeter telescopes are commonly used to confirm the planetary nature of transiting candidates identified by TESS. These light curves are used to confirm that the transit-like feature occurs on the particular star of interest, and not on another star inside the photometric aperture of the TESS data. Given the low number of transits present in TESS data for the three systems presented in this study, these additional light curves are also crucial for refining the photometric ephemeris. The observations were obtained in the context of the TESS follow-up program (TFOP) subgroup 1.

We used the Las Cumbres Observatory (LCO; Brown et al. 2013) network of telescopes to obtain follow-up light curves of TOI 4406 and TOI 2338. For this goal we used the LCO stations located in the South African Astronomical Observatory (SAAO), the Siding Spring Observatory (SSO), and CTIO. For TOI 4406 and TOI 2338 we also used data obtained with the Antarctic Search for Transiting ExoPlanets (ASTEP; Guillot et al. 2015) telescope installed in the Concordia station on the Antarctic continent. Likewise, for TOI 2338 and TOI 2589 we also used data obtained with two telescopes (CDK14 0.36 m and the OM-ES) installed in the El Sauce Observatory located in the Rio Hurtado province, in Chile. Finally, a full transit was obtained for TOI 2589 with the telescope of the Hazelwood observatory, in Australia.

The photometric observations were reduced and aperture photometry extraction was conducted using `AstroImageJ` (Collins et al. 2017) for all follow-up transit observations except for those of the OM-ES telescope that were based on automated routines previously used in other robotic telescopes (e.g., Jordán et al. 2019; Brahm et al. 2020).

All ground-based follow-up observations are summarized in Table 2, where we list the dates of observations, telescope apertures, passband filters, and exposure times. The light curves[42] are also presented in Figures 7, 8, and 9.
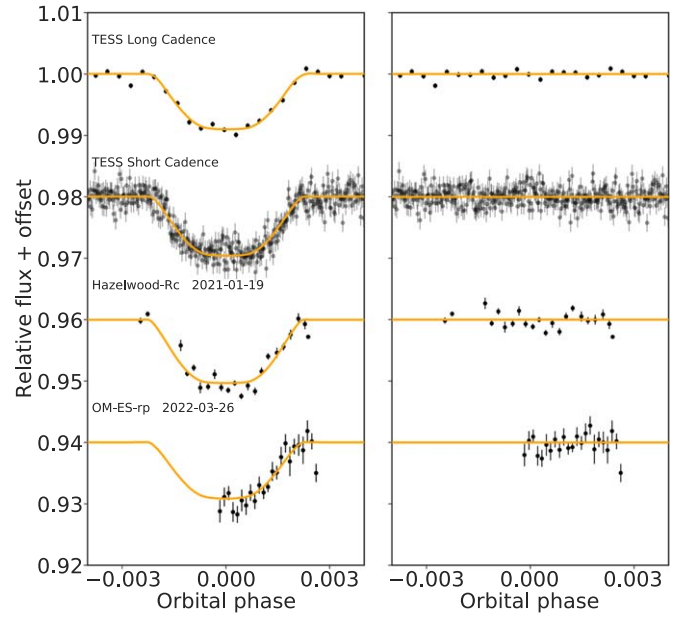
2.4. High-resolution Imaging

We used the optical speckle imaging technique for the three stars presented in this study. Specifically, the three stars were
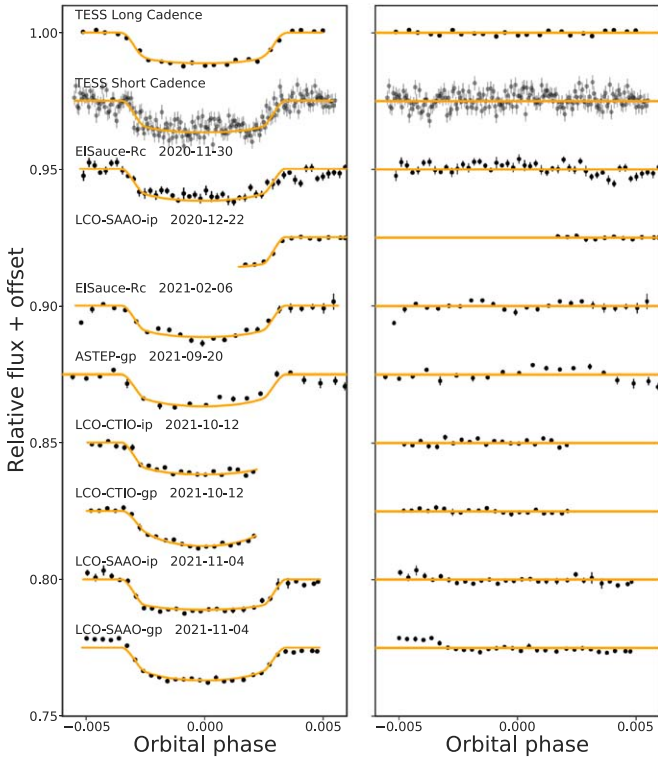
---

[42] The data can be downloaded from the ExoFOP platform (https://exofop.ipac.caltech.edu/tess/).
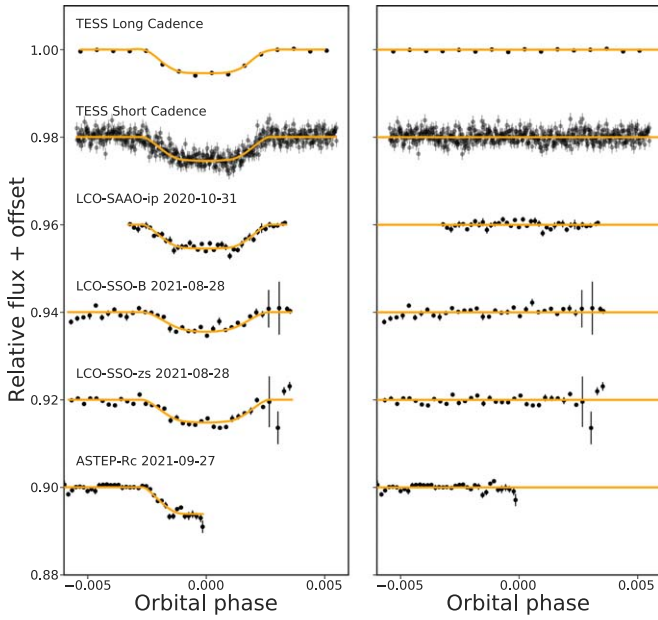
Figure 7. All photometric transits of TOI 4406b as a function of orbital phase obtained with TESS and ground-based facilities. Residuals are presented in the right panel.
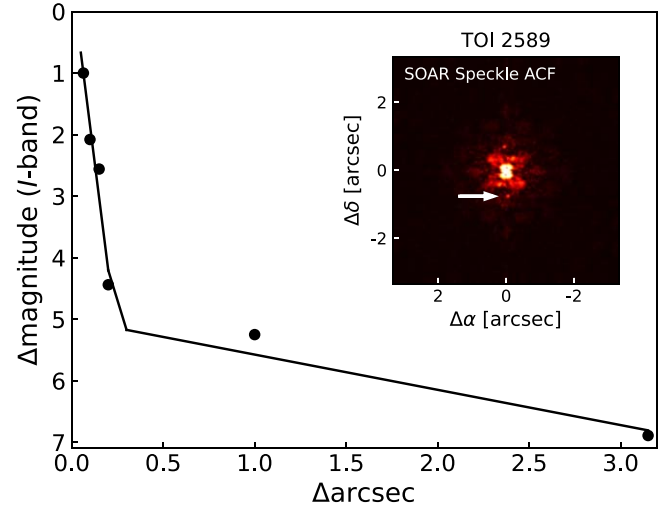

Figure 8. All photometric transits of TOI 2338b as a function of orbital phase obtained with TESS and ground-based facilities. No detrending was performed on the ground-based light curves, which generates a negative slope in the residuals of LCO-SAAO.

Figure 9. All photometric transits of TOI 2589b as a function of orbital phase obtained with TESS and ground-based facilities.

Figure 10. Contrast curve of TOI 2589 obtained with the Speckle imaging facility HRCam at SOAR. The image inset shows the faint companion star (marked with a white arrow). The additional feature above the star is the same companion mirrored in the autocorrelation function, a product of the speckle image reduction.

faint neighbor ($\Delta I = 3$ mag) at $0\rlap{.}{''}7$ was identified (see Figure 10). The flux associated with the neighboring star might impact the determination of the physical parameters of the host star and the planetary transit parameters by diluting the transits. These effects are taken into account in the analysis of the TOI 2338 system presented in Section 3.

3. Analysis

3.1. Stellar Parameters

We determined the parameters of the three stars presented in this study following the same iterative procedure adopted in previous discoveries of the WINE collaboration (e.g., Schlecker et al. 2020; Hobson et al. 2021). The atmospheric

observed with HRCam of the Southern Astrophysical Research (SOAR) telescope (Tokovinin 2018; Ziegler et al. 2020). Observations were performed on 2020-12-03, 2021-10-01, and 2021-11-20 for TOI 2338, TOI 4406, and TOI 2589, respectively. No nearby companions were identified for TOI 4406 and TOI 2338 with a contrast of $\Delta I = 7$ mag at $1''$. For TOI 2589 a

Table 3
Stellar Properties[a] of TOI 4406, TOI 2338, and TOI 2589

Parameter	TOI 4406	TOI 2338	TOI 2589[b]	Reference
Names	TIC 206541859	TIC 24358417	TIC 157698565	TICv8
	2MASS J01121157−5655316	2MASS J05252264−3440059	2MASS J07095718−3713515	2MASS
	TYC 8477-00008-1	TYC 7063-00698-1	TYC 7102-00426-1	TYCHO
R.A. (J2015.5)	$01^{h}12^{m}11\overset{s}{.}64$	$05^{h}25^{m}22\overset{s}{.}7$	$07^{hm}57\overset{s}{.}16$	Gaia DR2
decl. (J2015.5)	$-56^{d}55^{m}31\overset{s}{.}39$	$-34^{d}40^{m}05\overset{s}{.}7$	$-37^{d}13^{m}51\overset{s}{.}41$	Gaia DR2
pm$^{\text{R.A.}}$ (mas yr^{-1})	34.48 ± 0.04	38.00 ± 0.03	-18.98 ± 0.04	Gaia DR2
pm$^{\text{decl.}}$ (mas yr^{-1})	19.11 ± 0.04	18.02 ± 0.03	8.32 ± 0.04	Gaia DR2
π (mas)	3.79 ± 0.03	3.16 ± 0.02	4.96 ± 0.02	Gaia DR2
T (mag)	10.566 ± 0.006	11.702 ± 0.006	10.721 ± 0.006	TICv8
B (mag)	11.61 ± 0.11	13.144 ± 0.43	11.904 ± 0.18	APASS[c]
V (mag)	10.937 ± 0.007	12.483 ± 0.03	11.415 ± 0.012	APASS
G (mag)	10.955 ± 0.008	12.186 ± 0.023	11.196 ± 0.006	Gaia DR2[d]
G_{BP} (mag)	11.256 ± 0.005	12.581 ± 0.018	11.580 ± 0.008	Gaia DR2
G_{RP} (mag)	10.519 ± 0.009	11.653 ± 0.023	10.672 ± 0.009	Gaia DR2
J (mag)	10.034 ± 0.024	11.076 ± 0.026	10.071 ± 0.022	2MASS[e]
H (mag)	9.769 ± 0.025	10.746 ± 0.025	9.693 ± 0.026	2MASS
K_s (mag)	9.730 ± 0.023	10.664 ± 0.025	9.632 ± 0.021	2MASS
T_{eff} (K)	6219 ± 70	5581 ± 60	5579 ± 70	This work
$\log g$ (dex)	4.29 ± 0.02	4.40 ± 0.02	$4.35^{+0.02}_{-0.01}$	This work
[Fe/H] (dex)	0.10 ± 0.05	0.22 ± 0.04	0.12 ± 0.04	This work
$v \sin i$ (km s^{-1})	4.5 ± 0.3	2.5 ± 0.3	2.2 ± 0.3	This work
$M_\star$ ($M_\odot$)	1.19 ± 0.03	$0.99^{+0.03}_{-0.02}$	$0.93^{+0.03}_{-0.02}$	This work
$R_\star$ ($R_\odot$)	1.29 ± 0.01	1.05 ± 0.01	1.07 ± 0.01	This work
$L_\star$ ($L_\odot$)	2.3 ± 0.1	$0.97^{+0.04}_{-0.03}$	$0.99^{+0.04}_{-0.03}$	This work
en qA_V (mag)	0.17 ± 0.06	$0.07^{+0.06}_{-0.05}$	$0.11^{+0.06}_{-0.05}$	This work
Age (Gyr)	2.9 ± 0.7	7 ± 2	11^{+2}_{-2}	This work
$\rho_\star$ (g cm^{-3})	0.78 ± 0.03	1.22 ± 0.07	1.07 ± 0.07	This work

Notes.
[a] The stellar parameters computed in this work do not consider possible systematic differences among different stellar evolutionary models (Tayar et al. 2022) and have underestimated uncertainties.
[b] We note that the magnitudes reported for TOI 2589 include the contamination of a close neighbor ($\Delta I = 2.9$ mag).
[c] Munari et al. (2014).
[d] Gaia Collaboration et al. (2018).
[e] Skrutskie et al. (2006).

parameters are computed from the co-added FEROS spectra using the ZASPE code (Brahm et al. 2017b), which compares the observed spectra with a grid of synthetic ones. The results of this code are the effective temperature (T_{eff}), surface gravity ($\log g$), metallicity ([Fe/H]), and projected rotational velocity ($v \sin i$) of the corresponding star. These results include uncertainties that include the systematic mismatch between the data and the best-fit synthetic model. The physical stellar parameters are then computed by comparing public broadband photometric magnitudes of each star with those produced by the PARSEC stellar evolutionary models (Bressan et al. 2012). In this process we make use of the Gaia DR2 (Gaia Collaboration et al. 2018) parallax of each star to transform the observed magnitudes to absolute magnitudes. We also fix the metallicity of the stellar models to the value found with ZASPE, while the ZASPE effective temperature is used as a prior. We use the emcee package (Foreman-Mackey et al. 2013) to obtain the distributions for the stellar mass ($M_\star$), stellar age, and interstellar extinction (A_V). From these distributions, and using the stellar models, we also derive distributions for the stellar radius ($R_\star$), stellar luminosity ($L_\star$), stellar density ($\rho_\star$), and a new value for the surface gravity ($\log g$). This new $\log g$ value is more constrained than the spectroscopic one, and therefore the iterative process starts by

repeating the spectroscopic algorithm fixing the $\log g$ value to the one obtained with the evolutionary models, which is followed by a new run of the evolutionary models. We repeat this procedure until convergence is reached for the $\log g$ value, which usually occurs in less than four iterations. The reported stellar uncertainties on the stellar parameters are internal and do not consider possible systematic differences among different stellar evolutionary models, resulting in underestimated uncertainties (Tayar et al. 2022).

We performed a special analysis for TOI 2589 to incorporate the contamination of the faint companion in the broadband photometry. First, we considered the faint companion as a gravitational bound object to TOI 2589 and incorporated a new source with the same metallicity and distance to the analysis presented in the previous paragraph. This analysis did not deliver a good fit to the spectral energy distribution, where the best-fit model for the companion star presented significant excess flux in the reddest magnitudes. For this reason, we decided to perform a more detailed analysis where we assumed that the companion star was a chance alignment. To do this, we carried out a blend analysis following the procedures described in Hartman et al. (2019). We performed a joint modeling of the light curves, the radial velocity observations, the broadband photometry measurements, the measured I-band magnitude

Table 4
Prior and Posterior Parameters of the Global Analysis of TOI 4406b

Parameter	Prior	Value
P (days)	$N(30.1, 0.1)$	$30.08364^{+0.00005}_{-0.00005}$
T_0 (BJD)	$N(2458372.19, 0.01)$	$2458372.194^{0.001}_{0.001}$
$\rho_\star$ (kg m^{-3})	$N(776, 60)$	784^{+48}_{-49}
$R_P/R_\star$	$U(0.001, 1)$	$0.079^{+0.001}_{-0.001}$
b	$U(0, 1)$	$0.887^{+0.008}_{-0.008}$
K (km s^{-1})	$U(0, 0.2)$	$0.017^{+0.002}_{-0.002}$
e	$U(0, 0.9)$	$0.15^{+0.05}_{-0.04}$
ω	$(0, 360)$	39^{+18}_{-15}
q_1^{TESS}	$U(0, 1)$	$0.3^{+0.1}_{-0.1}$
q_2^{TESS}	$U(0, 1)$	$0.6^{+0.2}_{-0.3}$
$q_1^{\text{LCO}-\text{SAAO}-\text{ip}}$	$U(0, 1)$	$0.2^{+0.1}_{-0.1}$
$q_2^{\text{LCO}-\text{SAAO}-\text{ip}}$	$U(0, 1)$	$0.7^{+0.2}_{-0.3}$
$q_1^{\text{LCO}-\text{SSO}-\text{zs}}$	$U(0, 1)$	$0.6^{+0.1}_{-0.1}$
$q_1^{\text{LCO}-\text{SSO}-\text{B}}$	$U(0, 1)$	$0.94^{+0.04}_{-0.07}$
$q_1^{\text{ASTEP}-\text{Rc}}$	$U(0, 1)$	$0.1^{+0.1}_{-0.1}$
$\sigma_w^{\text{TESS,S2}}$ (ppm)	$LU(10^{-1}, 10^3)$	204^{+14}_{-15}
$\sigma_w^{\text{TESS,S28}}$ (ppm)	$LU(10^{-1}, 10^3)$	3^{+17}_{-2}
$\sigma_w^{\text{TESS,S29}}$ (ppm)	$LU(10^{-1}, 10^3)$	8^{+63}_{-7}
$\sigma_w^{\text{LCO}-\text{SAAO}-\text{ip}}$ (ppm)	$LU(10^{-1}, 10^4)$	1190^{+110}_{-110}
$\sigma_w^{\text{LCO}-\text{SSO}-\text{zs}}$ (ppm)	$LU(10^{-1}, 10^4)$	1250^{+140}_{-130}
$\sigma_w^{\text{LCO}-\text{SSO}-\text{B}}$ (ppm)	$LU(10^{-1}, 10^4)$	1410^{+140}_{-120}
$\sigma_w^{\text{ASTEP}-\text{Rc}}$ (ppm)	$LU(10^{-1}, 10^4)$	610^{+210}_{-520}
$\mu_{\text{flux}}^{\text{TESS,28}}$ (ppm)	$N(0, 0.1)$	$-0.00002^{+0.00001}_{-0.00001}$
$\mu_{\text{flux}}^{\text{TESS,29}}$ (ppm)	$N(0, 0.1)$	$-0.00003^{+0.00001}_{-0.00001}$
$\mu_{\text{flux}}^{\text{LCO}-\text{SAAO}-\text{ip}}$ (ppm)	$N(0, 0.1)$	$-0.002^{+0.0002}_{-0.0002}$
$\mu_{\text{flux}}^{\text{LCO}-\text{SSSO}-\text{zs}}$ (ppm)	$N(0, 0.1)$	$-0.0017^{+0.0002}_{-0.0002}$
$\mu_{\text{flux}}^{\text{LCO}-\text{SSO}-\text{B}}$ (ppm)	$N(0, 0.1)$	$-0.0014^{+0.0002}_{-0.0002}$
$\mu_{\text{flux}}^{\text{ASTEP}-\text{Rc}}$ (ppm)	$N(0, 0.1)$	$-0.0008^{+0.0001}_{-0.0001}$
γ_{CHIRON} (km s^{-1})	$N(0.00, 0.03)$	$-0.01^{+0.01}_{-0.01}$
γ_{CORALIE} (km s^{-1})	$N(24.19, 0.03)$	$24.184^{+0.007}_{-0.007}$
γ_{FEROS} (km s^{-1})	$N(24.18, 0.03)$	$24.191^{+0.004}_{-0.004}$
γ_{HARPS} (km s^{-1})	$N(24.18, 0.03)$	$24.187^{+0.002}_{-0.002}$
σ_{CHIRON} (km s^{-1})	$N(0.001, 0.1)$	$0.01^{+0.02}_{-0.01}$
σ_{CORALIE} (km s^{-1})	$N(0.001, 0.1)$	$0.002^{+0.005}_{-0.001}$
σ_{FEROS} (km s^{-1})	$N(0.001, 0.1)$	$0.015^{+0.004}_{-0.003}$
σ_{HARPS} (km s^{-1})	$N(0.001, 0.1)$	$0.004^{+0.002}_{-0.001}$
$\sigma_{\text{TESS,2}}^{\text{GP}}$	$LU(10^{-5}, 10^5)$	$-0.0008^{+0.0001}_{-0.0001}$
$\rho_{\text{TESS,2}}^{\text{GP}}$	$LU(10^{-3}, 10^3)$	$2.0^{+0.5}_{-0.4}$
$a/R_\star$		$33.5^{+0.7}_{-0.7}$
i (deg)		$88.48^{+0.04}_{-0.04}$
M_P (M_J)		$0.30^{+0.03}_{-0.03}$
R_P (R_J)		$1.00^{+0.02}_{-0.02}$
a (au)		$0.201^{+0.005}_{-0.005}$
T_{eq}(K)		904^{+16}_{-17}

Note. For the priors, $N(\mu, \sigma)$ stands for a normal distribution with mean μ and standard deviation σ, $U(a, b)$ stands for a uniform distribution between a and b, and $LU(a, b)$ stands for a log-uniform prior defined between a and b. The stellar parameters, from which the planetary parameters are derived, do not consider possible systematic differences among different stellar evolutionary models (Tayar et al. 2022) and have underestimated uncertainties.

difference between the bright planet host and the neighboring star, the spectroscopically determined stellar atmospheric parameters, and the astrometric parallax from Gaia. We varied as free parameters the mass, age, metallicity, and distance of the planet-hosting star; the mass, impact parameter, eccentricity

and argument of periastron, and radius of the planet; and the mass, age, metallicity, and distance of the companion star. We also varied the limb-darkening coefficients and various light-curve detrending parameters. We placed a prior of [Fe/H] $= 0.0 \pm 0.5$ dex on the metallicity of the neighboring star and set priors on the limb-darkening coefficients based on the tabulations from Claret et al. (2012, 2013) and Claret (2018). We used the MIST v1.2 stellar evolution models (Paxton et al. 2011, 2013, 2015; Choi et al. 2016; Dotter 2016) to determine the radius, luminosity, temperature, and absolute magnitudes of the stars given the varied parameters, and we assumed a line-of-sight Galactic extinction based on the MWDUST package (Bovy et al. 2016). Based on this analysis, we find that the physical properties of the neighboring star are not very well constrained, but the dilution contributed to each bandpass from the neighbor is fairly well constrained. We find that the neighbor has a mass of $1.34^{+0.43}_{-0.48}$ $M_\odot$, is at a distance modulus of $10.29^{+0.63}_{-1.40}$ mag, has an age of $0.80^{+2.57}_{-0.61}$ Gyr, and has a metallicity of [Fe/H] $= -0.86^{+0.45}_{-0.39}$ dex, where there are significant correlations between these parameters. Having the stellar parameters for the companion star, we included them as an additional source in the PARSEC stellar analysis of TOI 2589.

The stellar parameters obtained with the procedure mentioned in the previous paragraphs are presented in Table 3. TOI 4406 is a late F-type star ($T_{\text{eff}} = 6219 \pm 70$ K), slightly metal-rich ([Fe/H] $= 0.10 \pm 0.05$ [dex]), with a mass of $M_\star = 1.19 \pm 0.03$ $M_\odot$ and a radius of $R_\star = 1.29 \pm 0.01$ $R_\odot$. On the other hand, TOI 2338 and TOI 2589 are G-type stars, with effective temperatures of $T_{\text{eff}} = 5581 \pm 60$ K and $T_{\text{eff}} = 5552 \pm 70$ K, respectively. TOI 2338 has a metallicity of [Fe/H] $= 0.22 \pm 0.04$ [dex], a mass of $M_\star = 0.99 \pm 0.03$ $M_\odot$, and a radius of $R_\star = 1.05 \pm 0.01$ $R_\odot$. TOI 2589 has a metallicity of [Fe/H] $= 0.12 \pm 0.04$ [dex], a mass of $M_\star = 0.93 \pm 0.02$ $M_\odot$, and a radius of $R_\star = 1.07 \pm 0.01$ $R_\odot$. The inclusion of the companion for TOI 2589 in the analysis changes the stellar mass and radius of the target star by 1 standard deviation.

3.2. Global Modeling

For each system we simultaneously model TESS photometry, ground-based light curves, and precision radial velocities with the `juliet` package (Espinoza et al. 2019). `juliet` searches the global posterior maximum by computing the Bayesian log evidence ($\ln \zeta$) with a nested-sampling algorithm. `juliet` uses the `radvel` package (Fulton et al. 2018) to model the radial velocities, while the photometric transits are modeled with `batman` (Kreidberg 2015). In this study we use the `dynesty` (Speagle 2020) package incorporated in `juliet` to perform the posterior sampling with 500 live points. For TESS 30 m cadence data we used the oversampling technique to model the transit light curves (Kipping 2010). For the three systems presented in this analysis we adopt the stellar density as a free parameter of the transit model instead of the $a/R_\star$ parameter, and we use the density derived from the stellar analysis as a Gaussian prior for this parameter. We note that the stellar parameters do not include uncertainty from systematic differences among different stellar evolutionary models, resulting in underestimated uncertainties on planetary parameters.
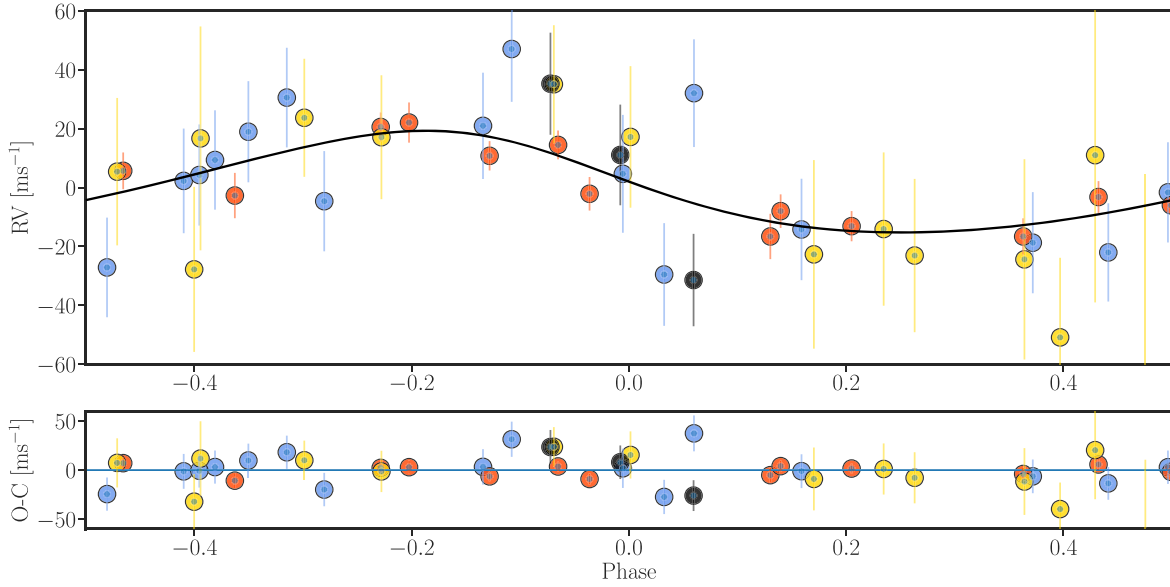
Figure 11. Radial velocities of TOI 4406 as a function of the orbital phase of TOI 4406b (FEROS: blue; Coralie: yellow; CHIRON: black; HARPS: orange). The solid line corresponds to the Keplerian model using the posterior parameters of the joint fit.

3.2.1. Global Modeling of TOI 4406b

For the analysis of TOI 4406b we use the 30 m cadence light curve of sector 2 computed with tesseract, the PDCSAP light curves of sectors 28 and 29, and all four ground-based photometric light curves. For TESS we adopt the quadratic limb-darkening law, where both parameters were set as free parameters with uniform priors between 0 and 1. For the ground-based light curves, we adopt the linear limb-darkening law with uniform priors between 0 and 1 for each telescope. We also include a Gaussian process to model systematic variations present in the 30 m cadence light curve of sector 2, for which we use a Matern 3/2 kernel. In addition to the photometry, we use the CHIRON, CORALIE, FEROS, and HARPS radial velocities as data and model them with a simple Keplerian model. We also consider distinct radial velocity zero-points and jitter factors for each instrument as free parameters. We tried two different models for TOI 4406b with juliet. First, we forced a circular orbit by fixing the eccentricity to 0, and then we considered a model with the eccentricity and argument of the periastron as free parameters. Even though the eccentricity is not strongly constrained, the eccentric model was strongly favored (17 times more likely) when comparing the Bayesian log-evidences of both models.

The prior distributions, along with the resulting parameters for the adopted model for TOI 4406b, are presented in Table 4. Figure 11 presents the phase-folded radial velocities along with the Keplerian model using the parameters obtained from the posterior distributions. TOI 4406b is a warm giant planet with a mass of $M_P = 0.30^{+0.02}_{-0.03} M_J$ and a radius of $R_P = 1.00^{+0.02}_{-0.02} R_J$. It has a low-eccentricity orbit ($e = 0.15 \pm 0.05$) with a period of 30.0836 days and a time-averaged equilibrium temperature of 903 ± 15 K (assuming zero albedo and uniform planet surface temperature; Méndez & Rivera-Valentín 2017).

3.2.2. Global Modeling of TOI 2338b

For the global modeling of TOI 2338b we used the TESS 30 m cadence light curves of sectors 5 and 6 and the 2 m cadence light curve of sector 32, as well as the ground-based follow-up

light curves. To model the TESS light curves, we adopted the quadratic limb-darkening law, while ground-based light curves were modeled with the linear limb-darkening law. Two distinct Gaussian processes were adopted for modeling the TESS light curves of sectors 5 and 6. A Matern 3/2 kernel was used in both cases. We modeled the HARPS and FEROS radial velocities of TOI 2338 with an eccentric Keplerian signal. Distinct zero-points and jitter terms were used for modeling each instrument.

The prior distributions along with the resulting parameters for the adopted model of TOI 2338b are presented in Table 5. Figure 12 presents the phase-folded radial velocities for TOI 2338b along with the Keplerian model using the parameters obtained from the posterior distributions. TOI 2338b is a massive warm giant planet with a mass of $M_P = 5.98^{+0.020}_{-0.21} M_J$ and a radius of $R_P = 1.00^{+0.02}_{-0.02} R_J$. It has a highly eccentric orbit of $e = 0.676 \pm 0.002$ with a period of 22.65398 ± 0.00002 days and a time-averaged equilibrium temperature of 799 ± 10 K.

3.2.3. Global Modeling of TOI 2589b

For the global modeling of TOI 2589b we adopted the quadratic limb-darkening law for the TESS light curves of sectors 7 and 34 and the linear limb-darkening law for the ground-based light curves. TESS data were also modeled with a distinct Gaussian process for each sector with a Matern 3/2 kernel. For the ground-based light curve obtained with the Hazelwood Observatory we included a linear model where the air mass was user as the linear regressor. For modeling the radial velocities we adopted an eccentric Keplerian signal, with different radial velocity zero-points and jitter terms for each instrument. For the ground-based light curves and the TESS light curve of sector 34 we included the contamination of the faint companion by considering fixed dilution factors of 0.92 and 0.93, respectively. These dilution factors were computed from the magnitudes of the faint companion star obtained from the analysis presented in Section 3.1. For the TESS light curve of sector 7, we adopted a uniform prior for the dilution factor to allow for additional contaminating sources.

Table 5
Prior and Posterior Parameters of the Global Analysis of TOI 2338b

Parameter	Prior	Value
P (days)	$N(22.7, 0.1)$	$22.65398^{+0.00002}_{-0.00002}$
T_0 (BJD)	$N(2458458.8, 0.2)$	$2458458.7545^{+0.0008}_{-0.0008}$
$\rho_\star$ (kg m^{-3})	$N(1120, 90)$	1301^{+51}_{-58}
$R_P/R_\star$	$U(0.001, 1)$	$0.0980^{+0.0008}_{-0.0008}$
b	$U(0, 1)$	$0.26^{+0.06}_{-0.06}$
K (km s^{-1})	$U(0.1, 2.0)$	$0.584^{+0.004}_{-0.004}$
e	$U(0, 0.9)$	$0.676^{+0.002}_{-0.002}$
ω (deg)	$(0, 360)$	$12.6^{+0.7}_{-0.6}$
$q_1^{\rm TESS}$	$U(0, 1)$	$0.4^{+0.2}_{-0.2}$
$q_2^{\rm TESS}$	$U(0, 1)$	$0.2^{+0.2}_{-0.1}$
$q_1^{\rm LCO-SAAO-ip}$	$U(0, 1)$	$0.4^{+0.1}_{-0.1}$
$q_1^{\rm ElSauce-Rc}$	$U(0, 1)$	$0.45^{+0.08}_{-0.08}$
$q_1^{\rm ASTEP-Rc}$	$U(0, 1)$	$0.5^{+0.1}_{-0.1}$
$q_1^{\rm LCO-SAAO-0.4m-ip}$	$U(0, 1)$	$0.47^{+0.07}_{-0.08}$
$q_1^{\rm LCO-SAAO-0.4m-gp}$	$U(0, 1)$	$0.88^{+0.05}_{-0.05}$
$q_1^{\rm LCO-CTIO-ip}$	$U(0, 1)$	$0.5^{+0.1}_{-0.1}$
$q_1^{\rm LCO-CTIO-gp}$	$U(0, 1)$	$0.73^{+0.06}_{-0.06}$
$\sigma_w^{\rm TESS,S5}$ (ppm)	$LU(10^{-1}, 10^3)$	370^{+30}_{-30}
$\sigma_w^{\rm TESS,S6}$ (ppm)	$LU(10^{-1}, 10^3)$	3^{+17}_{-2}
$\sigma_w^{\rm TESS,S32}$ (ppm)	$LU(10^{-1}, 10^3)$	4^{+32}_{-4}
$\sigma_w^{\rm LCO-SAAO-ip}$ (ppm)	$LU(10^{-1}, 10^4)$	590^{+100}_{-90}
$\sigma_w^{\rm ElSauce-Rc-1}$ (ppm)	$LU(10^{-1}, 10^4)$	10^{+150}_{-10}
$\sigma_w^{\rm ElSauce-Rc-2}$ (ppm)	$LU(10^{-1}, 10^4)$	70^{+940}_{-70}
$\sigma_w^{\rm ASTEP-Rc}$ (ppm)	$LU(10^{-1}, 10^4)$	2260^{+200}_{-180}
$\sigma_w^{\rm LCO-SAAO-0.4m-ip}$ (ppm)	$LU(10^{-1}, 10^4)$	1120^{+150}_{-130}
$\sigma_w^{\rm LCO-SAAO-0.4m-gp}$ (ppm)	$LU(10^{-1}, 10^4)$	1100^{+120}_{-110}
$\sigma_w^{\rm LCO-CTIO-ip}$ (ppm)	$LU(10^{-1}, 10^4)$	1760^{+200}_{-190}
$\sigma_w^{\rm LCO-CTIO-gp}$ (ppm)	$LU(10^{-1}, 10^4)$	1490^{+150}_{-140}
$\mu_{\rm dil}^{\rm TESS,S5}$	$U(0.5, 1.0)$	$0.986^{+0.009}_{-0.016}$
$\mu_{\rm dil}^{\rm TESS,S6}$	$U(0.5, 1.0)$	$0.989^{+0.008}_{-0.012}$
$\mu_{\rm flux}^{\rm TESS,S32}$ (ppm)	$N(0, 0.1)$	$0.00001^{+0.00002}_{-0.00002}$
$\mu_{\rm flux}^{\rm LCO-SAAO-ip}$ (ppm)	$N(0, 0.1)$	$-0.0008^{+0.0001}_{-0.0001}$
$\mu_{\rm flux}^{\rm ElSauce-Rc-1}$ (ppm)	$N(0, 0.1)$	$-0.004^{+0.0003}_{-0.0003}$
$\mu_{\rm flux}^{\rm ElSauce-Rc-2}$ (ppm)	$N(0, 0.1)$	$-0.0061^{+0.0002}_{-0.0002}$
$\mu_{\rm flux}^{\rm ASTEP-Rc}$ (ppm)	$N(0, 0.1)$	$-0.0045^{+0.0002}_{-0.0002}$
$\mu_{\rm flux}^{\rm LCO-SAAO-0.4m-ip}$ (ppm)	$N(0, 0.1)$	$-0.0095^{+0.0002}_{-0.0002}$
$\mu_{\rm flux}^{\rm LCO-SAAO-0.4m-gp}$ (ppm)	$N(0, 0.1)$	$-0.0105^{+0.0002}_{-0.0002}$
$\mu_{\rm flux}^{\rm LCO-CTIO-ip}$ (ppm)	$N(0, 0.1)$	$-0.0077^{+0.0002}_{-0.0002}$
$\mu_{\rm flux}^{\rm LCO-CTIO-gp}$ (ppm)	$N(0, 0.1)$	$-0.0080^{+0.0002}_{-0.0002}$
$\sigma_{\rm FEROS}$ (km s^{-1})	$N(0.001, 0.1)$	$0.020^{+0.006}_{-0.004}$
$\sigma_{\rm HARPS}$ (km s^{-1})	$N(0.001, 0.1)$	$0.003^{+0.003}_{-0.002}$
$\gamma_{\rm FEROS}$ (km s^{-1})	$N(83.92, 0.03)$	$83.926^{+0.006}_{-0.005}$
$\gamma_{\rm HARPS}$ (km s^{-1})	$N(83.95, 0.03)$	$83.942^{+0.002}_{-0.002}$
$a/R_\star$		$32.3^{+0.6}_{-0.6}$
i (deg)		$89.52^{+0.02}_{-0.02}$
M_P ($M_{\rm J}$)		$5.98^{+0.21}_{-0.20}$
R_P ($R_{\rm J}$)		$1.00^{+0.02}_{-0.02}$
a (au)		$0.158^{+0.003}_{-0.003}$
$T_{\rm eq}$(K)		799^{+10}_{-11}

Note. See Table 4 for the definition of prior distributions. The stellar parameters, from which the planetary parameters are derived, do not consider possible systematic differences among different stellar evolutionary models (Tayar et al. 2022) and have underestimated uncertainties.

The prior distributions, along with the resulting parameters for the adopted model of TOI 2589b, are presented in Table 6. Figure 13 presents the phase-folded radial velocities for TOI

Table 6
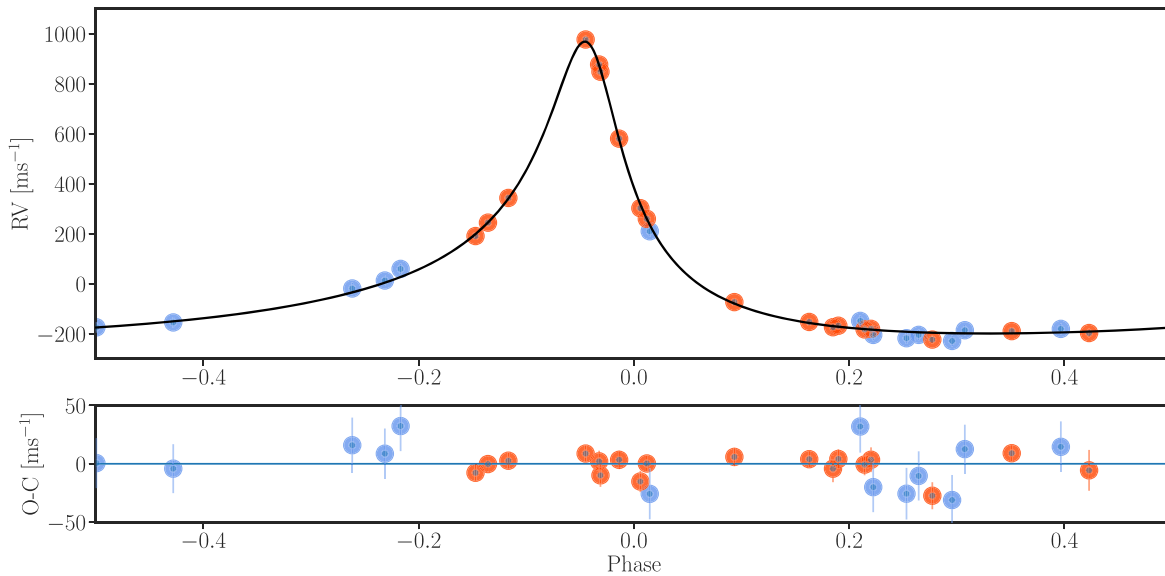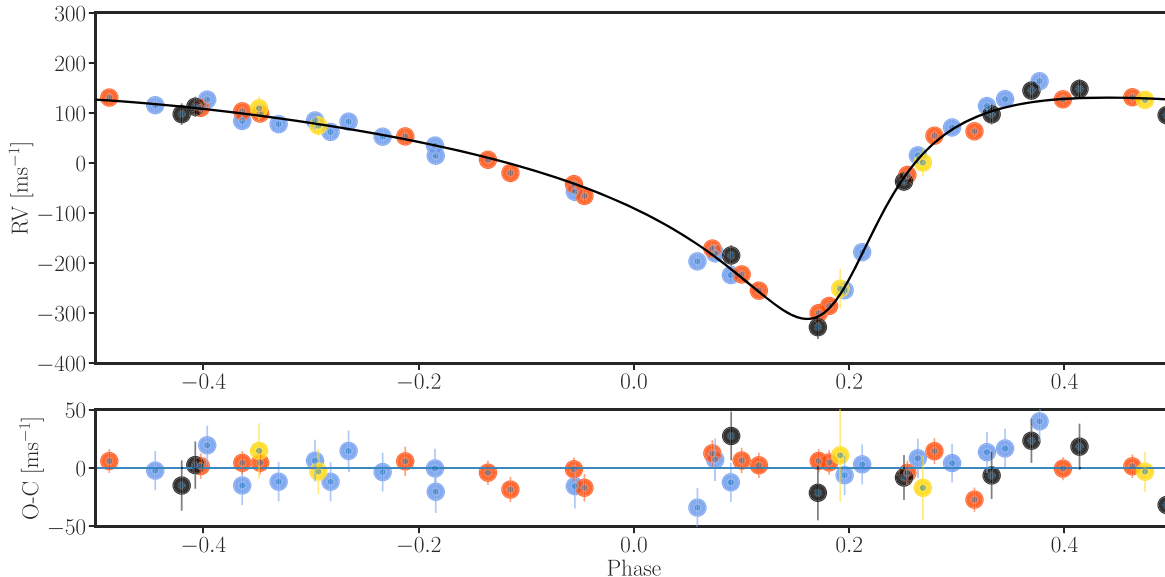Prior and Posterior Parameters of the Global Analysis of TOI 2589b

Parameter	Prior	Value
P (days)	$N(61.6, 0.5)$	$61.6277^{+0.0002}_{-0.0002}$
T_0 (BJD)	$N(2458494.6, 0.2)$	$2458494.579^{+0.002}_{-0.002}$
$\rho_\star$ (kg m^{-3})	$N(1070, 70)$	1140^{+50}_{-50}
$R_P/R_\star$	$U(0.001, 1)$	$0.107^{+0.003}_{-0.003}$
b	$U(0, 1)$	$0.878^{+0.006}_{-0.008}$
K (km s^{-1})	$U(0.15, 0.30)$	$0.221^{+0.003}_{-0.003}$
e	$U(0, 0.9)$	$0.522^{+0.006}_{-0.006}$
ω	$(0, 360)$	218^{+1}_{-1}
$q_1^{\rm TESS}$	$U(0, 1)$	$0.14^{+0.10}_{-0.08}$
$q_2^{\rm TESS}$	$U(0, 1)$	$0.8^{+0.2}_{-0.2}$
$q_1^{\rm HWD}$	$U(0, 1)$	$0.2^{+0.2}_{-0.1}$
$q_1^{\rm OM-ES}$	$U(0, 1)$	$0.5^{+0.3}_{-0.3}$
$\sigma_w^{\rm TESS,S7}$ (ppm)	$LU(10^{-1}, 10^3)$	480^{+20}_{-20}
$\sigma_w^{\rm TESS,S34}$ (ppm)	$LU(10^{-1}, 10^3)$	4^{+50}_{-4}
$\sigma_w^{\rm HWD}$ (ppm)	$LU(10^{-1}, 10^4)$	1890^{+150}_{-140}
$\sigma_w^{\rm OM-ES}$ (ppm)	$LU(10^{-1}, 10^4)$	10^{+220}_{-10}
$\mu_{\rm flux}^{\rm HWD}$ (ppm)	$N(0, 0.1)$	$-0.015^{+0.002}_{-0.002}$
$\mu_{\rm flux}^{\rm OM-ES}$ (ppm)	$N(0, 0.1)$	$-0.006^{+0.001}_{-0.001}$
$\mu_{\rm dil}^{\rm TESS,S7}$	$U(0.7, 1.0)$	$0.94^{+0.03}_{-0.03}$
$\sigma_{\rm CHIRON}$ (km s^{-1})	$LU(0.001, 0.1)$	$0.018^{+0.007}_{-0.005}$
$\sigma_{\rm FEROS}$ (km s^{-1})	$LU(0.001, 0.1)$	$0.015^{+0.003}_{-0.003}$
$\sigma_{\rm HARPS}$ (km s^{-1})	$LU(0.001, 0.1)$	$0.010^{+0.002}_{-0.002}$
$\sigma_{\rm CORALIE}$ (km s^{-1})	$LU(0.001, 0.1)$	$0.001^{+0.0046}_{-0.0008}$
$\gamma_{\rm CHIRON}$ (km s^{-1})	$N(-1.80, 0.05)$	$-1.805^{+0.007}_{-0.007}$
$\gamma_{\rm FEROS}$ (km s^{-1})	$N(68.55, 0.03)$	$68.549^{+0.004}_{-0.004}$
$\gamma_{\rm HARPS}$ (km s^{-1})	$N(68.58, 0.03)$	$65.579^{+0.002}_{-0.002}$
$\gamma_{\rm CORALIE}$ (km s^{-1})	$N(68.58, 0.03)$	$68.566^{+0.009}_{-0.009}$
$\sigma_{\rm TESS,S7}^{\rm GP}$	$LU(10^{-5}, 10^4)$	$0.0009^{+0.006}_{-0.0003}$
$\rho_{\rm TESS,S7}^{\rm GP}$	$LU(10^{-5}, 10^4)$	4^{+3}_{-2}
$\sigma_{\rm TESS,S34}^{\rm GP}$	$LU(10^{-5}, 10^4)$	$0.00019^{+0.00006}_{-0.00004}$
$\rho_{\rm TESS,S34}^{\rm GP}$	$LU(10^{-5}, 10^4)$	$2.2^{+0.9}_{-0.6}$
$\theta_0^{\rm HWD}$	$U(-1, 1)$	$-0.007^{+0.001}_{-0.001}$
$a/R_\star$		$61.2^{+0.9}_{-0.9}$
i (deg)		$89.17^{+0.01}_{-0.01}$
M_P ($M_{\rm J}$)		$3.5^{+0.1}_{-0.1}$
R_P ($R_{\rm J}$)		$1.08^{+0.03}_{-0.03}$
a (au)		$0.300^{+0.006}_{-0.005}$
$T_{\rm eq}$(K)		592^{+7}_{-8}

Note. See Table 4 for the definition of prior distributions. The stellar parameters, from which the planetary parameters are derived, do not consider possible systematic differences among different stellar evolutionary models (Tayar et al. 2022) and have underestimated uncertainties.

2589b along with the Keplerian model using the parameters obtained from the posterior distributions. TOI 2589b is a long-period ($P = 61.6277 \pm 0.0002$ days) warm Jupiter with a mass of $M_P = 3.5^{+0.01}_{-0.1}$ $M_{\rm J}$ and a radius of $R_P = 1.09^{+0.03}_{-0.03}$ $R_{\rm J}$. It has a moderately large orbital eccentricity of $e = 0.523 \pm 0.006$ and a time-averaged equilibrium temperature of 593 ± 8 K.

3.3. Search for Additional Signals

We searched for additional periodic signals in the TESS light curves of the three stars presented in this study. For each Presearch Data Conditioning Simple Aperture Photometry (PDCSAP; Smith et al. 2012; Stumpe et al. 2014) light curve with a cadence of 120 s, we removed outliers, masked the

Figure 12. Radial velocities of TOI 2338 as a function of the orbital phase of TOI 2338b (FEROS: blue; HARPS: orange). The solid line corresponds to the Keplerian model using the posterior parameters of the joint fit.


Figure 13. Radial velocities of TOI 2589 as a function of the orbital phase of TOI 2589b (FEROS: blue; CHIRON: black; HARPS: orange; CORALIE: yellow). The solid line corresponds to the Keplerian model using the posterior parameters of the joint fit.

known transits and applied a generalized Lomb−Scargle (GLS) periodogram (Zechmeister & Kürster 2009) to identify possible sinusoidal variations produced by the rotation of the stars. We found no significant signals for any of the three systems. After that, we also applied a box-fitting least-squares (BLS; Kovács et al. 2002) search for detecting periodic transits produced by smaller planetary companions, but no significant signals were found either.

We also searched for additional signals in the radial velocities. We ran a GLS periodogram on the residuals of the radial velocities for each system, finding no significant peaks in the corresponding power spectra. Additionally, we included a radial velocity linear trend in the global modeling of each system, but the Bayesian evidences obtained for these models were lower than those of the models not including the linear trend in the radial velocities.

Finally, we explored the possibility of identifying long-period companions from Gaia astrometric excess noise, but the three systems presented in this study have proper-motion uncertainties consistent with other stars having similar magnitudes and parallaxes.

3.4. Heavy-element Content

We estimate the amount of heavy elements for the three warm Jupiters following the procedure described in Sarkis et al. (2021). We compare the planetary radius obtained from the evolution model `completo21` (Mordasini et al. 2012) with the observed radius, while varying the heavy-element content of the envelope. `completo21` has been validated through the modeling of the formation and evolution of Jupiter in the core accretion framework, and the models are in agreement with results presented in Burrows et al. (1997) and Baraffe et al.
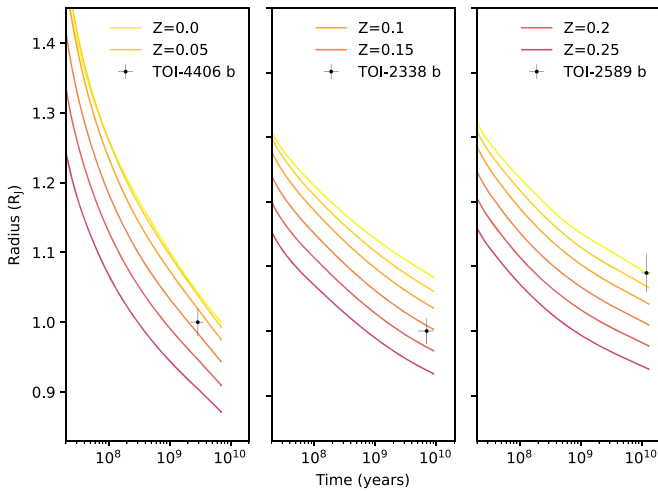
Figure 14. Evolution curves of the planetary radius as a function of time color-coded by the water mass fraction of the envelope. The points correspond to the current properties of each planet.

(2003). Completo21 is used to model the core and the envelope and is coupled with a semi-gray atmospheric model (Guillot 2010). We chose the SCvH equation of states of hydrogen and helium and a helium mass fraction of $Y = 0.27$ (Saumon et al. 1995). The models of TOI 4406b and TOI 2338b contain a core of 10 $M_\oplus$ (Thorngren et al. 2016) composed of iron and silicates with an iron mass fraction of 33%. The relatively large radius of TOI 2589b is compatible with no heavy-element enrichment; hence, we chose not to include a core for this planet. The heavy elements outside the core are modeled by the AQUA2020 equation of state of water (Haldemann et al. 2020) and are assumed to be homogeneously mixed in the envelope. All planets are modeled from 10 Myr up to past their current age determination. Figure 14 displays the resulting evolution curves of the planetary radius for several water mass fractions in the envelope (Z). We derive error estimates on the water mass fraction by a simple Monte Carlo approach combining the planetary radius and stellar age uncertainties, as done in Ulmer-Moll et al. (2022). The parameters of TOI 4406b, TOI 2338b, and TOI 2589b are well explained by a total mass of heavy elements of $21^{+5}_{-5} M_\oplus$, $330^{+60}_{-60} M_\oplus$, and $40^{+50}_{-40} M_\oplus$, which corresponds to a total heavy-element mass fraction of (Z_p) of $0.23^{+0.05}_{-0.05}$, $0.174^{+0.031}_{-0.031}$, and $0.03^{+0.04}_{-0.03}$, respectively. Assuming that the stellar metallicity scales with the iron abundance (Asplund et al. 2009; Miller & Fortney 2011), the heavy-element enrichments of the planets are $12.6^{+3.1}_{-3.1}$ for TOI 4406b, $7.4^{+1.5}_{-1.5}$ for TOI 2338b, and $1.9^{+2.3}_{-1.9}$ for TOI 2589b. TOI 4406b and TOI 2338b are significantly metal-enriched planets, while TOI 2589b is consistent with no heavy-element enrichment.

4. Discussion

TOI 4406b, TOI 2338b, and TOI 2589b are three transiting Jovian planets with predicted time-averaged equilibrium temperatures below 1000 K and orbital periods between 22 and 62 days and can therefore be classified as warm Jupiters. Figure 15 puts these discoveries in the context of the full population of transiting giant planets, highlighting the relative scarcity of systems with periods longer than 10 days, which is produced mostly by observational biases. TOI 2589b, with an orbital period of 61.6 days, is currently among the five longest-period confirmed planets identified by the TESS mission.

Transiting warm Jupiters, due to the mild irradiation levels experienced from their parent stars, allow for the study of their internal bulk structures without the need to consider proximity effects. In our case, the three transiting warm Jupiters have significantly different masses but similar radii, which is expected given the electron degeneracy pressure for noninflated envelopes (Zapolsky & Salpeter 1969). The right panel of Figure 16 corresponds to the mass–radius diagram for the population of transiting warm giant planets from the TEPCat catalog (Southworth 2011). While hot Jupiters have radii well above the predictions based on classical planetary structural models, warm Jupiters have radii similar to or below ≈ 1 R_J.

The metal enrichment of these three new planets is consistent with the correlation presented in Thorngren et al. (2016), where lower-mass giant planets are more enriched in metals relative to their stars if compared with the more massive giant planets. In this study, we find that the Saturn-mass planet TOI 4406b is significantly more enriched in metals relative to its star than the two super-Jupiters TOI 2338b and TOI 2589b. While we find that the most massive planet of our sample (TOI 2338b) has a higher relative enrichment than the less massive super-Jupiter TOI 2589b, this deviation is consistent with the moderate scatter presented in the Thorngren et al. (2016) correlation. TOI 2338b and TOI 2589b have very similar stellar hosts, and the difference in their internal composition favors the hypothesis that the final structural composition of massive planets is not fully constrained by the properties of the star but is significantly dependent on specific formation histories. The structure of TOI 2589b is consistent with a coreless interior and an envelope with a stellar-like metal enrichment. These properties can be associated with the gravitational instability formation mechanism, but the mass of TOI 2589b is below the 10 M_J boundary proposed by Schlaufman (2018) above which objects orbiting solar-type dwarf stars are expected to have been formed by this process. If TOI 2589b was formed by the core accretion mechanism, then it was able to accrete all the available gas in its feeding zone.

TOI 2338b and TOI 2589b stand out owing to their large orbital eccentricities (see left panel of Figure 16), while TOI 4406b has an almost circular orbit. As opposed to hot Jupiters, the population of warm Jupiters is known for having a wide distribution of orbital eccentricities (Winn & Fabrycky 2015). The eccentricities can be linked to formation scenarios of close-in giant planets (e.g., Dong et al. 2021a).

In situ formation of hot and warm Jupiters presents theoretical challenges. While growth through planetesimal accretion is fast owing to the short orbital timescales, the narrow feeding zones of available material in the inner system are typically depleted before a sufficient core mass can be reached (Lissauer 1993). Additional accretion of millimeter-to-centimeter-sized pebbles (Ormel & Klahr 2010) can grow a solid core more efficiently (Batygin et al. 2016), but pebble isolation (e.g., Lambrechts et al. 2014) limits attainable core masses on close orbits to values too low for runaway gas accretion (Lin et al. 2018).

An alternative scenario is that these planets form beyond the snowline and then migrate inward through interaction with the gaseous disk (Goldreich & Tremaine 1980; Kley & Nelson 2012). Given an appropriate combination of solid disk mass and initial orbital distance of the emerging planetary nucleus, a gas giant on sub-au orbits can form in this way (Schlecker et al. 2021).
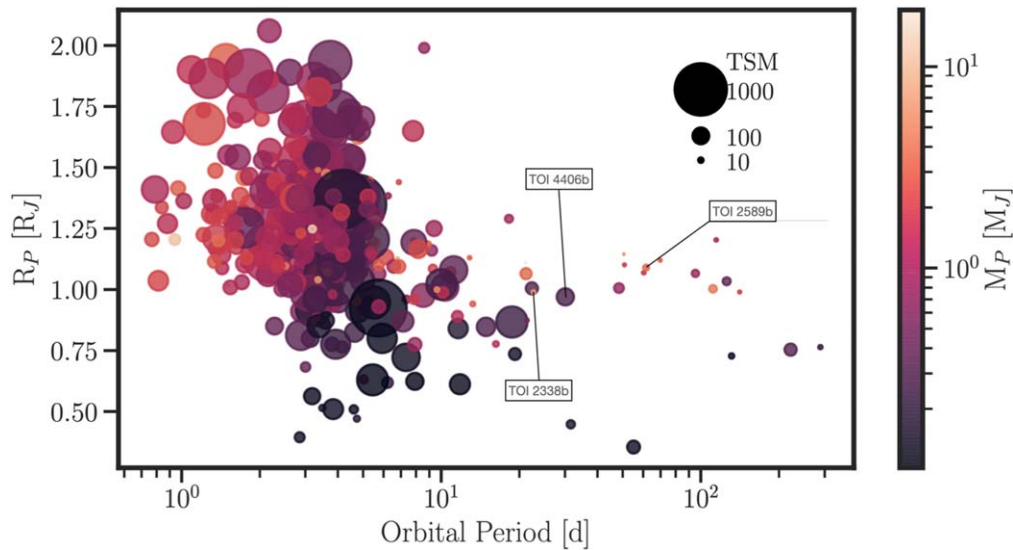
Figure 15. Planet radius vs. orbital period diagram for the population of transiting giant planets, color-coded by planet mass. The size of the circles scales with the transit spectroscopy metric (TSM; Kempton et al. 2018). The three systems presented in this study stand out owing to their relatively long periods.
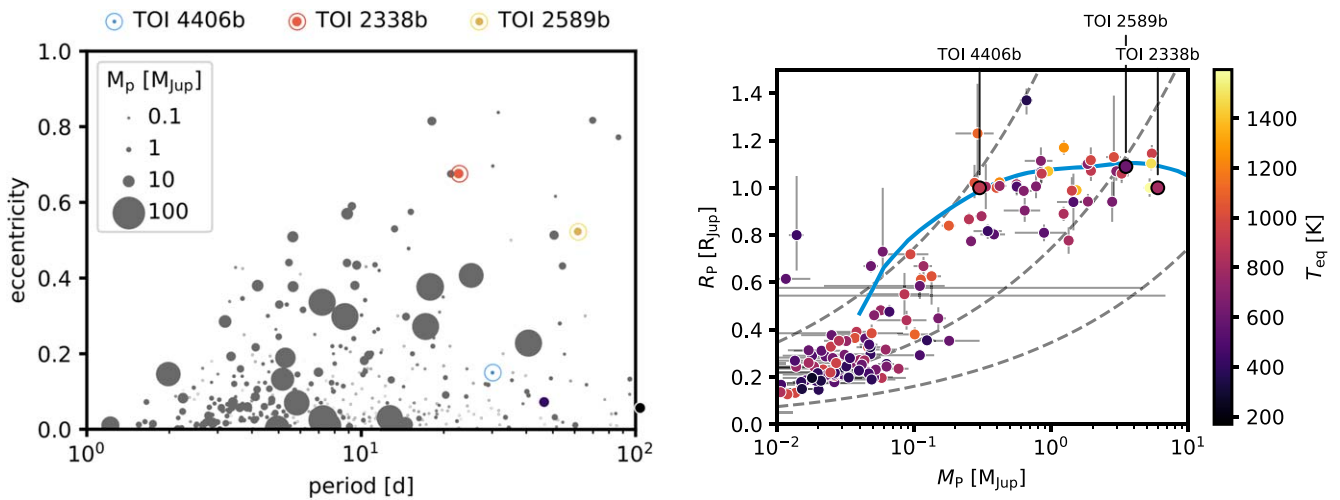
Figure 16. Left panel: orbital eccentricity as a function of orbital period for the population of transiting giant planets with a period of up to 100 days. TOI 2338b and TOI 2589b are among the few discovered planets with $e > 0.5$, with TOI 2338b being in the 98th percentile of the eccentricity distribution. Right panel: planet radius as a function of the planet mass for the population of warm giant planets ($P > 10$ days). Dashed gray lines correspond to bulk densities of 0.3, 3, and 30 g cm^{-3}. All three planets presented in this study have radii close to those predicted by standard structural models (Fortney et al. 2007, blue line).

Another mode to form large, close-in planets is excitation of the orbital eccentricities through dynamical interactions followed by orbital shrinking due to tides with the central star (Goldreich & Soter 1966). Dong et al. (2021b) recently announced the discovery of a possible hot Jupiter progenitor, a massive warm Jupiter with a highly eccentric orbit (TOI-3362b). While TOI 2338b has similar orbital and physical parameters to TOI-3362b, its eccentricity is currently not high enough to eventually end up as a hot Jupiter. Assuming a constant angular momentum path (e.g., Socrates et al. 2012), TOI 2338b is expected to attain a final semimajor axis of $a(1 - e^2) \approx 0.08$, but the timescale associated with that process is longer than the lifetime of the star (Adams & Laughlin 2006). This finding is similar to that for TIC 237913194b (Schlecker et al. 2020), which has a similar configuration to TOI 2338b and whose tidal evolution has been shown to be too slow for a hot Jupiter progenitor.

Under the current orbital configurations, the three planets presented in this study are not expected to become hot Jupiters.

Nonetheless, their locations inside the snowline require an explanation because they need to have experienced significant migration to reach their current semimajor axis. High-eccentricity migration mechanisms triggered by secular gravitational interactions have been proposed as a possible origin for the population of warm Jupiters (e.g., Socrates et al. 2012; Petrovich & Tremaine 2016; Anderson & Lai 2017; Mustill et al. 2017). In this scenario, an outer companion periodically modifies the orbital eccentricity and inclination of the inner warm Jupiter, and the migration is only significant in the high-eccentricity stages, when the pericenter distances are small enough to allow for strong tidal interactions that reduce the semimajor axes of the orbit. The large eccentricities of TOI 2338b and TOI 2589b indicate that they could be experiencing such secular cycles. On the other hand, the small orbital eccentricity of TOI 4406b is consistent with having experienced disk migration until reaching its current position.

Dong et al. (2014) pointed out that in order for warm Jupiters to be migrating through Kozai–Lidov oscillations triggered by

an outer Jovian mass companion, this second planet must be located at relatively close orbital distance in order to overcome the oscillation-suppressing effect of general relativity (Fabrycky & Tremaine 2007; Liu et al. 2015). Such companions should be detectable in long-term radial velocity monitoring of these systems. Jackson et al. (2021) predicted that such radial velocity trends induced by the outer perturbers should be detectable in a time span of 3 yr. Both eccentric systems presented in this study have been monitored for 3 yr, but no trend has been detected, ruling out the existence of an important fraction of possible perturbers. An extended and more precise radial velocity monitoring of these systems will be required to firmly reject the existence of outer perturbers that could be responsible for the migration.

In the absence of such close perturbers, the current orbital configurations of TOI 2338b and TOI 2589b can be explained by an initial stage of migration through the disk of systems composed of multiple giant planets, followed by a stage of scattering between the planets after the disk disperses. Based on N-body experiments, Anderson et al. (2020) show that the majority of eccentric warm Jupiters with no detected companions can be explained by this in situ scattering process, which supports this avenue for the current orbital state of TOI 2338b and TOI 2589b.

A crucial test to constrain the origin of the warm Jupiters presented in this study is through the measurement of their orbital inclinations. Specifically, migration through secular mechanisms predicts significant inclinations between the orbital plane of the warm Jupiter and the spin of the star (stellar obliquity). The sky-projected stellar obliquity can be obtained with radial velocity measurements during transit through the observation of the Rossiter–McLaughlin (R-M) effect (e.g., Sedaghati et al. 2021; Dong et al. 2022). The expected maximum radial velocity amplitude of the R-M effect is similar for the three systems. We predict amplitudes of the R-M signals for TOI 4406b and TOI 2589b of ≈ 9 m s^{-1}, for aligned orbits. For TOI 2338b, due to the smaller impact parameter of its transit, we predict a slightly larger signal of 16 m s^{-1} in the aligned case. The transit duration in all three cases (shorter than 7 hr) should allow for the spectroscopic observation of a full transit in a single night. A significant obliquity value for any of the three systems would further favor the high-eccentricity migration scenario triggered by secular gravitational interactions with outer companions as the cause of the close-in orbits (Petrovich & Tremaine 2016). Rice et al. (2022b) found a tendency toward spin–orbit alignment of warm-Jupiter systems and suggest it as evidence of distinct migration mechanisms for the hot- and warm-Jupiter populations. The obliquity measurement of a bigger sample of warm Jupiters, particularly those that are eccentric like TOI 2338b and TOI 2589b, will help in confirming this claim.

Formation and migration scenarios of giant planets can also be constrained by studying their atmospheric compositions (e.g., Öberg et al. 2011; Mordasini et al. 2016; Mollière et al. 2022). For example, Madhusudhan et al. (2014) inferred that high-eccentricity migration after disk dissipation can lead to substellar carbon and oxygen abundances with stellar or superstellar C/O abundance ratios. Planetary atmospheric abundances can be constrained with transmission spectroscopy measurements and also with the observation of the emission spectrum during secondary eclipses. The compact nature of TOI 2338b and TOI 2589b does not favor atmospheric studies

in transmission, but emission studies would be possible. TOI 4406b, on the other hand, is a well-suited target for both transmission and emission studies owing to its lower density. As can be noted in Figure 15, TOI 4406b has currently the highest transmission spectroscopy metric (Kempton et al. 2018) for giant planets with periods longer than 20 days.

publicly available from the Mikulski Archive for Space Telescopes (MAST).

Facilities: TESS, Gaia, LCO, El Sauce, ASTEP, Hazelwood Observatory, SOAR, ESO 3.6 m, MPG 2.2 m, SMARTS 1.5 m, Euler-Swiss telescope 1.2 m.

Software: astropy (Astropy Collaboration et al. 2013), ceres (Brahm et al. 2017a), AstroImageJ (Collins et al. 2017), zaspe (Brahm et al. 2017b), juliet (Espinoza et al. 2019), batman (Kreidberg 2015), radvel (Fulton et al. 2018), emcee (Foreman-Mackey et al. 2013), dynesty (Speagle 2020).

ORCID iDs

Rafael Brahm ● https://orcid.org/0000-0002-9158-7315
Solène Ulmer-Moll ● https://orcid.org/0000-0003-2417-7006
Melissa J. Hobson ● https://orcid.org/0000-0002-5945-7975
Andrés Jordán ● https://orcid.org/0000-0002-5389-3944
Thomas Henning ● https://orcid.org/0000-0002-1493-300X
Trifon Trifonov ● https://orcid.org/0000-0002-0236-775X
Martin Schlecker ● https://orcid.org/0000-0001-8355-2107
Nestor Espinoza ● https://orcid.org/0000-0001-9513-1449
Felipe I. Rojas ● https://orcid.org/0000-0003-3047-6272
Pascal Torres ● https://orcid.org/0000-0003-0974-210X
Paula Sarkis ● https://orcid.org/0000-0001-8128-3126
Jan Eberhardt ● https://orcid.org/0000-0003-3130-2768
Diana Kossakowski ● https://orcid.org/0000-0002-0436-7833
Diego J. Muñoz ● https://orcid.org/0000-0003-2186-234X
Joel D. Hartman ● https://orcid.org/0000-0001-8732-6166
Vincent Suc ● https://orcid.org/0000-0001-7070-3842
François Bouchy ● https://orcid.org/0000-0002-7613-393X
Guillaume Chaverot ● https://orcid.org/0000-0003-4711-3099
Monika Lendl ● https://orcid.org/0000-0001-9699-1459
Olga Suarez ● https://orcid.org/0000-0002-3503-3617
Tristan Guillot ● https://orcid.org/0000-0002-7188-8428
Amaury H. M. J. Triaud ● https://orcid.org/0000-0002-5510-8751
Nicolas Crouzet ● https://orcid.org/0000-0001-7866-8738
Georgina Dransfield ● https://orcid.org/0000-0002-3937-630X
Ryan Cloutier ● https://orcid.org/0000-0001-5383-9393
Khalid Barkaoui ● https://orcid.org/0000-0003-1464-9276
Rick P. Schwarz ● https://orcid.org/0000-0001-8227-1020
Chris Stockdale ● https://orcid.org/0000-0003-2163-1437
Mallory Harris ● https://orcid.org/0000-0002-3721-1683
Ismael Mireles ● https://orcid.org/0000-0002-4510-2268
Phil Evans ● https://orcid.org/0000-0002-5674-2404
Andrew W. Mann ● https://orcid.org/0000-0003-3654-1602
Diana Dragomir ● https://orcid.org/0000-0003-2313-467X
Steven Villanueva ● https://orcid.org/0000-0001-6213-8804
Christoph Mordasini ● https://orcid.org/0000-0002-1013-2811
George Ricker ● https://orcid.org/0000-0003-2058-6662
Roland Vanderspek ● https://orcid.org/0000-0001-6763-6562
David W. Latham ● https://orcid.org/0000-0001-9911-7388
Sara Seager ● https://orcid.org/0000-0002-6892-6948
Joshua N. Winn ● https://orcid.org/0000-0002-4265-047X
Jon M. Jenkins ● https://orcid.org/0000-0002-4715-9460
Allison Youngblood ● https://orcid.org/0000-0002-1176-3391
Tansu Daylan ● https://orcid.org/0000-0002-6939-9211
Karen A. Collins ● https://orcid.org/0000-0001-6588-9574
Douglas A. Caldwell ● https://orcid.org/0000-0003-1963-9616
David R. Ciardi ● https://orcid.org/0000-0002-5741-3047
Enric Palle ● https://orcid.org/0000-0003-0987-1593
Felipe Murgas ● https://orcid.org/0000-0001-9087-1245

References

Adams, F. C., & Laughlin, G. 2006, ApJ, 649, 1004
Albrecht, S., Winn, J. N., Johnson, J. A., et al. 2012, ApJ, 757, 18
Almenara, J. M., Damiani, C., Bouchy, F., et al. 2015, A&A, 575, A71
Anderson, K. R., & Lai, D. 2017, MNRAS, 472, 3692
Anderson, K. R., Lai, D., & Pu, B. 2020, MNRAS, 491, 1369
Asplund, M., Grevesse, N., Sauval, A. J., & Scott, P. 2009, ARA&A, 47, 481
Astropy Collaboration, Robitaille, T. P., Tollerud, E. J., et al. 2013, A&A, 558, A33
Bakos, G. Á., Noyes, R. W., Kovács, G., et al. 2007, ApJ, 656, 552
Baraffe, I., Chabrier, G., Barman, T. S., Allard, F., & Hauschildt, P. H. 2003, A&A, 402, 701
Baranne, A., Queloz, D., Mayor, M., et al. 1996, A&AS, 119, 373
Batygin, K., Bodenheimer, P. H., & Laughlin, G. P. 2016, ApJ, 829, 114
Bovy, J., Rix, H.-W., Green, G. M., Schlafly, E. F., & Finkbeiner, D. P. 2016, ApJ, 818, 130
Brahm, R., Espinoza, N., Jordán, A., et al. 2019, AJ, 158, 45
Brahm, R., Jordán, A., Bakos, G. Á., et al. 2016, AJ, 151, 89
Brahm, R., Jordán, A., & Espinoza, N. 2017a, PASP, 129, 034002
Brahm, R., Jordán, A., Hartman, J., & Bakos, G. 2017b, MNRAS, 467, 971
Brahm, R., Nielsen, L. D., Wittenmyer, R. A., et al. 2020, AJ, 160, 235
Bressan, A., Marigo, P., Girardi, L., et al. 2012, MNRAS, 427, 127
Brown, T. M., Baliber, N., Bianco, F. B., et al. 2013, PASP, 125, 1031
Burrows, A., Marley, M., Hubbard, W. B., et al. 1997, ApJ, 491, 856
Chachan, Y., Dalba, P. A., Knutson, H. A., et al. 2022, ApJ, 926, 62
Chatterjee, S., Ford, E. B., Matsumura, S., & Rasio, F. A. 2008, ApJ, 686, 580
Choi, J., Dotter, A., Conroy, C., et al. 2016, ApJ, 823, 102
Claret, A. 2018, A&A, 618, A20
Claret, A., Hauschildt, P. H., & Witte, S. 2012, A&A, 546, A14
Claret, A., Hauschildt, P. H., & Witte, S. 2013, A&A, 552, A16
Collins, K. A., Kielkopf, J. F., Stassun, K. G., & Hessman, F. V. 2017, AJ, 153, 77
Dalba, P. A., Kane, S. R., Dragomir, D., et al. 2022, AJ, 163, 61
Dalba, P. A., Kane, S. R., Isaacson, H., et al. 2021a, AJ, 161, 103
Dalba, P. A., Kane, S. R., Li, Z., et al. 2021b, AJ, 162, 154
Dawson, R. I., Huang, C. X., Brahm, R., et al. 2021, AJ, 161, 161
Dawson, R. I., & Johnson, J. A. 2018, ARA&A, 56, 175
Dong, J., Huang, C. X., Dawson, R. I., et al. 2021a, ApJS, 255, 6
Dong, J., Huang, C. X., Zhou, G., et al. 2021b, ApJL, 920, L16
Dong, J., Huang, C. X., Zhou, G., et al. 2022, ApJL, 926, L7
Dong, S., Katz, B., & Socrates, A. 2014, ApJL, 781, L5
Dotter, A. 2016, ApJS, 222, 8
Eisner, N. L., Nicholson, B. A., Barragán, O., et al. 2021, MNRAS, 505, 1827
Espinoza, N., Fortney, J. J., Miguel, Y., Thorngren, D., & Murray-Clay, R. 2017, ApJL, 838, L9
Espinoza, N., Kossakowski, D., & Brahm, R. 2019, MNRAS, 490, 2262
Fabrycky, D., & Tremaine, S. 2007, ApJ, 669, 1298
Foreman-Mackey, D., Hogg, D. W., Lang, D., & Goodman, J. 2013, PASP, 125, 306
Fortney, J. J., Marley, M. S., & Barnes, J. W. 2007, ApJ, 659, 1661
Fulton, B. J., Petigura, E. A., Blunt, S., & Sinukoff, E. 2018, PASP, 130, 044504
Gaia Collaboration, Brown, A. G. A., Vallenari, A., et al. 2018, A&A, 616, A1
Gill, S., Wheatley, P. J., Cooke, B. F., et al. 2020, ApJL, 898, L11
Goldreich, P., & Soter, S. 1966, Icar, 5, 375
Goldreich, P., & Tremaine, S. 1980, ApJ, 241, 425
Grieves, N., Bouchy, F., Ulmer-Moll, S., et al. 2022, A&A, 668, A29
Guillot, T. 2010, A&A, 520, A27
Guillot, T., Abe, L., Agabi, A., et al. 2015, AN, 336, 638
Haldemann, J., Alibert, Y., Mordasini, C., & Benz, W. 2020, A&A, 643, A105
Hartman, J. D., Bakos, G. Á., Bayliss, D., et al. 2019, AJ, 157, 55
Hobson, M. J., Brahm, R., Jordán, A., et al. 2021, AJ, 161, 235
Huang, C., Wu, Y., & Triaud, A. H. M. J. 2016, ApJ, 825, 98
Jackson, J. M., Dawson, R. I., Shannon, A., & Petrovich, C. 2021, AJ, 161, 200
Jenkins, J. M., Twicken, J. D., McCauliff, S., et al. 2016, Proc. SPIE, 9913, 99133E
Jones, M. I., Brahm, R., Espinoza, N., et al. 2019, A&A, 625, A16
Jordán, A., Brahm, R., Espinoza, N., et al. 2019, AJ, 157, 100

Jordán, A., Brahm, R., Espinoza, N., et al. 2020, AJ, 159, 145
Kaufer, A., Stahl, O., Tubbesing, S., et al. 1999, Msngr, 95, 8
Kempton, E. M. R., Bean, J. L., Louie, D. R., et al. 2018, PASP, 130, 114401
Kipping, D. M. 2010, MNRAS, 408, 1758
Kley, W., & Nelson, R. P. 2012, ARA&A, 50, 211
Kovács, G., Zucker, S., & Mazeh, T. 2002, A&A, 391, 369
Kreidberg, L. 2015, PASP, 127, 1161
Lambrechts, M., Johansen, A., & Morbidelli, A. 2014, A&A, 572, 1
Lin, D. N. C., & Papaloizou, J. 1986, ApJ, 309, 846
Lin, J. W., Lee, E. J., & Chiang, E. 2018, MNRAS, 480, 4338
Lissauer, J. J. 1993, ARA&A, 31, 129
Liu, B., Muñoz, D. J., & Lai, D. 2015, MNRAS, 447, 747
Madhusudhan, N., Amin, M. A., & Kennedy, G. M. 2014, ApJL, 794, L12
Mayor, M., Pepe, F., Queloz, D., et al. 2003, Msngr, 114, 20
Mayor, M., & Queloz, D. 1995, Natur, 378, 355
Méndez, A., & Rivera-Valentín, E. G. 2017, ApJL, 837, L1
Miller, N., & Fortney, J. J. 2011, ApJL, 736, L29
Mollière, P., Molyarova, T., Bitsch, B., et al. 2022, ApJ, 934, 74
Mordasini, C., Alibert, Y., Klahr, H., & Henning, T. 2012, A&A, 547, A111
Mordasini, C., van Boekel, R., Mollière, P., Henning, T., & Benneke, B. 2016, ApJ, 832, 41
Morton, T. D., & Johnson, J. A. 2011, ApJ, 729, 138
Munari, U., Henden, A., Frigo, A., et al. 2014, AJ, 148, 81
Mustill, A. J., Davies, M. B., & Johansen, A. 2017, MNRAS, 468, 3000
Öberg, K. I., Murray-Clay, R., & Bergin, E. A. 2011, ApJL, 743
Ormel, C. W., & Klahr, H. H. 2010, A&A, 520, A43
Paredes, L. A., Henry, T. J., Quinn, S. N., et al. 2021, AJ, 162, 176
Paxton, B., Bildsten, L., Dotter, A., et al. 2011, ApJS, 192, 3
Paxton, B., Cantiello, M., Arras, P., et al. 2013, ApJS, 208, 4
Paxton, B., Marchant, P., Schwab, J., et al. 2015, ApJS, 220, 15
Petrovich, C., & Tremaine, S. 2016, ApJ, 829, 132
Queloz, D., et al. 2001, The Messenger, 105, 1
Rasio, F. A., & Ford, E. B. 1996, Sci, 274, 954
Rice, M., Wang, S., & Laughlin, G. 2022a, ApJL, 926, L17

Rice, M., Wang, S., Wang, X.-Y., et al. 2022b, AJ, 164, 104
Ricker, G. R., Winn, J. N., Vanderspek, R., et al. 2015, JATIS, 1, 014003
Sarkis, P., Mordasini, C., Henning, T., Marleau, G. D., & Mollière, P. 2021, A&A, 645, A79
Saumon, D., Chabrier, G., & van Horn, H. M. 1995, ApJS, 99, 713
Schlaufman, K. C. 2018, ApJ, 853, 37
Schlecker, M., Kossakowski, D., Brahm, R., et al. 2020, AJ, 160, 275
Schlecker, M., Pham, D., Burn, R., et al. 2021, A&A, 656, A73
Sedaghati, E., MacDonald, R. J., Casasayas-Barris, N., et al. 2021, MNRAS, 505, 435
Skrutskie, M. F., Cutri, R. M., Stiening, R., et al. 2006, AJ, 131, 1163
Smith, J. C., Stumpe, M. C., Van Cleve, J. E., et al. 2012, PASP, 124, 1000
Socrates, A., Katz, B., Dong, S., & Tremaine, S. 2012, ApJ, 750, 106
Southworth, J. 2011, MNRAS, 417, 2166
Speagle, J. S. 2020, MNRAS, 493, 3132
Stevenson, D. J. 1982, P&SS, 30, 755
Stumpe, M. C., Smith, J. C., Catanzarite, J. H., et al. 2014, PASP, 126, 100
Tayar, J., Claytor, Z. R., Huber, D., & van Saders, J. 2022, ApJ, 927, 31
Thorngren, D. P., Fortney, J. J., Murray-Clay, R. A., & Lopez, E. D. 2016, ApJ, 831, 64
Tokovinin, A. 2018, PASP, 130, 035002
Tokovinin, A., Fischer, D. A., Bonati, M., et al. 2013, PASP, 125, 1336
Trifonov, T., Brahm, R., Espinoza, N., et al. 2021, AJ, 162, 283
Twicken, J. D., Catanzarite, J. H., Clarke, B. D., et al. 2018, PASP, 130, 064502
Ulmer-Moll, S., Lendl, M., Gill, S., et al. 2022, A&A, 666, A46
Winn, J. N., & Fabrycky, D. C. 2015, ARA&A, 53, 409
Wu, Y., & Lithwick, Y. 2011, ApJ, 735, 109
Zapolsky, H. S., & Salpeter, E. E. 1969, ApJ, 158, 809
Zechmeister, M., & Kürster, M. 2009, A&A, 496, 577
Ziegler, C., Tokovinin, A., Briceño, C., et al. 2020, AJ, 159, 19